Photocatalytic Activity Enhancement of Anatase/Rutile-Mixed Phase TiO_2 Nanoparticles Annealed with Low-Temperature O_2 Plasma

Retsuo Kawakami[*,1], Yuki Mimoto[1], Shin-ichiro Yanagiya[1], Akihiro Shirai[1], Masahito Niibe[2], Yoshitaka Nakano[3], and Takashi Mukai[4]

[1] *Graduate School of Technology, Industrial and Social Sciences, Tokushima University, Tokushima 770-8506, Japan*

[2] *Laboratory of Advanced Science and Technology for Industry, University of Hyogo, Kamigori, Hyogo 678-1205, Japan*

[3] *Chubu University, Kasugai, Aichi 487-8501, Japan*

[4] *Nichia Corporation, Anan, Tokushima 774-0044, Japan*

* Corresponding author. E-mail: retsuo@ee.tokushima-u.ac.jp, Phone: +81 88 656 7441, Fax: +81 88 656 7441

Abstract

Photodecomposition and photobactericidal activities of anatase/rutile-mixed phase TiO_2 nanoparticles annealed with low-temperature O_2 plasma were clarified by comparing them with those annealed in ambient air. The photocatalytic activities of plasma-assisted-annealed sample greatly enhanced as compared with the untreated sample, under not only ultraviolet irradiation but also visible-light irradiation. The photocatalytic activities of air-annealed samples did not enhance under ultraviolet irradiation but enhanced under visible-light irradiation. The enhanced photocatalytic activities due to the plasma-assisted annealing (PAA) originated from the increased photoexcited carrier concentration. This enhancement was discussed from PAA-induced characteristic factors. PAA facilitated the phase transformation to anatase, contributing directly to extending the photoexcited carrier lifetime. PAA introduced more oxygen vacancies, contributing to trapping more photogenerated electrons. PAA also introduced more bridging/terminal oxygen groups adsorbed on the surface, increasing the upward band-bending, the depletion layer width at the surface, and the charge transfer from rutile to anatase. These two introductions contributed to facilitating the separation of photoexcited carriers. Furthermore, PAA reduced the aggregate size of TiO_2 nanoparticles formed on the surface, contributing to increasing optical absorptions. More reactive oxygen species produced from the bridging/terminal oxygen groups by the photoexcited carriers would also enhance the photocatalytic activities.

Keywords: titanium oxide nanoparticles, anatase/rutile-mixed phases, plasma-assisted annealing, ambient air annealing, ultraviolet irradiation, visible-light irradiation, photocatalytic activity enhancement

1. Introduction

Titanium oxide (TiO_2) based photocatalysts have received much attention as an eco-friendly technology to prevent environmental pollution and bacterial contamination. This attention is that TiO_2-based photocatalysts have successfully decomposed various organic contaminants[1−5] and have efficaciously inactivated bacteria.[6−10] The use advantage of TiO_2 is that TiO_2 has high photocatalytic activity, high chemical stability, nontoxicity, excellent biocompatibility, and low cost compared with other metal oxide-based photocatalysts.[11−14] The photocatalytic activity of TiO_2 is driven by the irradiation of photons at energies larger than the bandgap energy of 3.0−3.2 eV (the bandgap wavelength of 388−415 nm). When these photons are absorbed by TiO_2, electrons and holes are generated at the conduction and valence bands, respectively. The photogenerated electrons reduce oxygen molecules, O_2, to superoxide anion radicals O_2^-. The photogenerated holes oxidize water, H_2O, to hydroxyl radicals, OH, and hydrogen ions, H^+. These hydrogen ions and the generated superoxide anion radicals can react to produce hydrogen peroxides, H_2O_2. These hydrogen peroxides are reduced to hydroxyl radicals by some photogenerated electrons. The photogenerated electrons and holes ultimately generate hydroxyl radicals playing a vital role in decomposing organic matters[15] and inactivating bacteria.[16] Thus, a prolonged lifetime of photoexcited carriers is highly required to enhance the photocatalytic activity.[17] Specifically, the recombination degree of photoexcited carriers needs to be greatly reduced for the enhanced photocatalytic activity. Understandably, increasing the amount of optical absorption is also important for enhancing the photocatalytic activity because it directly increases the photoexcited carrier concentration.

In general, the annealing treatment of TiO_2 in ambient air is a simple and effective post-treatment technology to enhance the photocatalytic activity.[18,19] The raised temperature of annealing not only enhances the crystallinity but also introduces more

oxygen vacancies into TiO_2. The introduced oxygen vacancies play an important role to enhance the photocatalytic activity of air-annealed TiO_2.[18,19] The introduced oxygen vacancies can trap the photogenerated electrons, lower the carrier recombination degree, and thus prolonging the carrier lifetime. This leads to the enhanced photocatalytic activity. For example, TiO_2 nanoparticles (NPs) called P-25 supplied by Degussa Co., Germany (hereinafter, they are referred to as P-25 NPs) are known to be often used as a criterion for evaluating the photocatalytic activities.[20–24] The feature of P-25 NPs is that P-25 NPs have photocatalytic activities under not only ultraviolet (UV) irradiation but also visible-light irradiation. This is because P-25 NPs consist of 80% anatase phase TiO_2 with a bandgap energy of 3.2 eV (a bandgap wavelength of 388 nm) and 20% rutile phase TiO_2 with a bandgap energy of 3.0 eV (a bandgap wavelength of 415 nm).[20–24] The photocatalytic activity of P-25 NPs under UV irradiation is reported to be enhanced by annealing in ambient air at a high temperature of 650 ℃ for a long time of 4 h.[25] The photocatalytic activity of P-25 NPs under visible-light irradiation is enhanced by annealing in ambient air at a high temperature of 800 ℃ for a long time of 3 h.[26] These enhancements are considered to be attributed to the annealing-induced oxygen vacancies.[25,26] However, these annealing treatment processes are often not practical because of both the high treatment temperature and the long treatment time required to enhancing the photocatalytic activities.

In the previous study, we have reported a low-temperature and short-time post-treatment technology for enhancing the photocatalytic activity of anatase phase TiO_2 NPs, i.e., O_2 plasma-assisted annealing at 300 ℃ for 1 h.[27] The anatase phase TiO_2 NPs called ST-01 supplied by Ishihara Sangyo, Japan were used in that study; hereinafter, they are referred to as ST-01 NPs. The technology of plasma-assisted annealing had the advantage that, in addition to the annealing-induced oxygen vacancies, more oxygen vacancies can be introduced into the anatase phase TiO_2 surface by plasma irradiation. The plasma-

assisted annealing enhanced the photodecomposition and photobactericidal activities of anatase phase TiO_2 NPs.[27] These photocatalytic activities were high compared with that of anatase phase TiO_2 NPs annealed in ambient air at various temperatures for 1 h. However, whether the plasma-assisted annealing contributes to enhancing the photocatalytic activities of TiO_2 NPs with other crystalline phases, i.e., anatase/rutile-mixed phase TiO_2 NPs, under not only UV irradiation but also visible-light irradiation remains unclear yet. This is of extreme importance for a deeper understanding of plasma-assisted annealing effect on the enhancement of UV and visible-light photocatalytic activities.

In the present study, the effects of O_2 plasma-assisted annealing on photocatalytic characteristics of anatase/rutile-mixed phase TiO_2 NPs have been investigated separately under UV irradiation and visible-light irradiation. For comparison, the effects of annealing in ambient air at various temperatures have also been investigated under the same light irradiation conditions. P-25 NPs were used as a representative for anatase/rutile-mixed phase TiO_2 NPs. A dielectric barrier discharge (DBD) plasma reactor equipped with a heater[27,28] was employed for the plasma-assisted annealing. An electric furnace was employed for the ambient air annealing. Photodecomposition of methylene blue (MB) dye in solution and photoinactivation of *Bacillus subtilis* American Type Culture Collection (*B. subtilis* ATCC) 6633[29] were evaluated for the UV and visible-light photocatalytic activities. 365-nm and 405-nm light-emitting-devices (LEDs) were employed for the UV and visible-light sources, respectively. The UV irradiation of P-25 NPs activates both the anatase and rutile phase crystals included in them. The visible-light irradiation activates only the rutile phase TiO_2 included in P-25 NPs. This is because the energy of 405-nm visible-light photons, 3.06 eV, is larger than the bandgap energy of rutile phase TiO_2, 3.0 eV, and smaller than the bandgap energy of anatase phase TiO_2, 3.2 eV. Changes in the sample crystallization behavior due to the post-treatment processes

were analyzed using X-ray diffraction (XRD). Changes in chemical compositions of the sample surfaces were examined by X-ray photoelectron spectroscopy (XPS). The photoexcited carrier concentrations were qualitatively assessed from a difference in electrical conductivities between light-irradiated and non-irradiated-samples. The plasma-assisted annealing effects on UV and visible-light photocatalytic activities are characterized by comparing the features of P-25 NPs exerted with the two post-treatment processes. The characteristics of plasma-assisted-annealed P-25 NPs in the present study and ST-01 NPs reported in the literature[27] are also compared. The present study is extremely essential for comprehensively understanding the enhancement mechanism of UV and visible-light photocatalytic activities of anatase/rutile-mixed phase TiO_2 NPs introduced by the plasma-assisted-annealing. The present study also demonstrates that the technology of plasma-assisted-annealing is greatly useful for the commercial and industrial fabrication of anatase/rutile-mixed phase TiO_2 NPs having high photodecomposition and photoinactivation under not only UV irradiation but also visible-light irradiation.

2. Experimental procedure

A detailed description of the experiment can be found in the literature.[27,28] The key elements are summarized in the following. A heater-equipped DBD plasma reactor was employed to investigate the plasma-assisted annealing effect of P-25 NPs, as in the case of ST-01 NPs.[27] Low-temperature O_2 plasma at atmospheric-pressure (100 kPa) was generated in a gap length of 2 mm between the electrically ground and powered disk electrodes in the DBD reactor while heating the electrically grounded electrode to a temperature of 300 °C. The diameters of these disk electrodes were the same, 40 mm. One side of the powered disk electrode was covered by a disk dielectric to keep the low-temperature plasma discharge at atmospheric-pressure. The disk dielectric was made of

alumina, and its size was 1 mm in thickness and 50 mm in diameter. The other side of the powered disk electrode was connected to a power supply generating a sinusoidal wave with a frequency of 25 kHz. O_2 gas (99.9 vol% purity) was fed from a high-pressure gas cylinder to the DBD reactor. The gas flow rate was kept constant at 15 ml/min. The maximum value of the applied voltage was set to 1.5 kV. In this case, the maximum value of the current flowing across the discharge gap was 100 mA. By integrating the multiplication of voltage and current waveforms over a single cycle, the consumed electric power was estimated to be 8 W.

The samples used were P-25 NPs immobilized on glass substrates with an area of 12.5 × 12.5 mm^2. The immobilization process of P-25 NPs was the same as that used in ST-01 NPs.[27] P-25 NPs were dispersed in deionized water and stirred for 1 h to prepare a TiO_2 dispersion solution with a concentration of 2.5×10^3 mass ppm. A 100 μl dispersion solution of P-25 NPs was dropped onto the glass surface after irradiating the glass surface with low-temperature Ar plasma generated at a gas pressure of 60 Pa in a capacitively-coupled plasma reactor.[30] The Ar plasma irradiation was performed for 10 min to effectively enhance the hydrophilicity of the glass surface. The dropped glass substrates were naturally dried at room temperature in the atmosphere for 24 h to prepare the samples. The thickness of immobilized P-25 NPs was approximately 400 nm as estimated from the mass density of P-25 NPs, 3.85 g/cm^3.[31] The prepared samples were put on the electrically grounded electrode of the DBD plasma reactor and then annealed for 1 h with the assistance of the O_2 plasma. For comparison, the samples were annealed in ambient air for 1 h with an electric furnace. The temperature of air-annealing was varied from 300 to 900 ℃ with an interval of 200 ℃. All the post-treated samples were irradiated with 365-nm UV at an intensity of 100 mW/cm^2 for 2 h to remove organic impurities from the surfaces.

The photodecomposition of MB dye was performed for evaluating UV and visible-

light photocatalytic activities of P-25 NPs. The UV source was a 365-nm light-emitted diode (LED, Nichia NVSU333A, Japan). The visible-light source was a 405-nm LED (Nichia NVSU119C, Japan). The UV and visible-light intensities at the sample surface were set to be the same, 10 mW/cm^2, as measured with an optical power meter (Ophir Nova II). Prior to light irradiation, the samples were dipped in 4 ml MB solution with a concentration of 10 mass ppm for 1 h under dark conditions to reach adsorption equilibrium. Then, the dipped samples were irradiated with 365-nm UV for 2 and 4 h, and with 405-nm visible-light for 4 and 8 h, respectively. A decrease in the MB dye concentration for each sample was measured by monitoring the absorbance peak intensity at a wavelength of 664 nm with a spectrophotometer (Otsuka Electronics Photal MCPD-370A, Japan) in the same manner as those reported in the literature.[32,33] The photodecomposition was measured three times for each sample and then the data were averaged.

The photoinactivation of *B. subtilis* ATCC 6633[29] was also evaluated under UV irradiation and visible-light irradiation, respectively. Firstly, the bacterial strains were grown in Luria-Bertani (LB) broth (Nacalai Tesque Lennox, Japan) at 37 ℃ with shaking at 160 rpm for 17 h. Then, the grown bacterial suspensions were centrifuged at 6570 *g* for 3 min at 4 ℃ to remove the LB broth, where *g* is the gravitational acceleration. Finally, the bacterial suspensions having 2×10^7 colony-forming units per ml (CFU/ml) were synthesized with sterile ion-exchanged water. After dropping a 0.01 ml bacterial suspension on the sample surface, the sample surface was irradiated with 365-nm UV emitted from a LED (Nichia NVSU233A, Japan) for 1 and 2 min and with 405-nm visible-light emitted from a LED (Nichia NVSU119C, Japan) for 2 and 4 min, respectively. The UV and visible-light intensities at the sample surface were set to be the same, 23.6 mW/cm^2, as measured with the same optical power meter. Immediately after light irradiation, the samples were homogenized in a 10 ml solution of soybean-casein

digest lecithin polysorbate (SCDLP, Nihon Pharmaceutica, Japan) broth for 1 min to extract the bacteria from the samples. A 0.1 ml broth suspension having bacteria was subjected to 10-fold serial dilutions with SCDLP broth. The serial dilutions were plated on agar plates of SCDLP and then incubated at 37 ℃ for 48 h. The common logarithm (log) numbers of viable cells grown on the plates after the incubation were evaluated with the colony counting method.[34,35] For comparison, the bactericidal experiments were performed in the absence of light irradiation. The photoinactivation of bacteria was measured three times for each sample and then the data were averaged.

Changes in the crystalline structures of samples induced by the plasma-assisted annealing were analyzed by using XRD (Rigaku RINT-2200/PC, Japan) with Cu Kα radiation. Changes in the surface morphologies were observed by using scanning electron microscopy (SEM, JEOL JSM-6510). Changes in the particle morphologies were observed by a field-emission scanning electron microscope (FE-SEM, Hitachi High-Technologies S-4700, Japan). Changes in the root mean square (RMS) surface roughness values were analyzed by using atomic force microscope (AFM, Hitachi High-Technologies AFM5500M, Japan). The AFM scanning area was 50 × 50 μm^2. Changes in the distribution of anatase and rutile phase TiO_2 crystals on the samples were measured with Raman spectromicroscopy (Nanophoton RAMAN-11, Japan). The Raman spectra from the samples were excited with an excitation laser of 532 nm in wavelength. The laser power was 120 mW, and the laser spot area was 500 μm^2. The Raman mapping images were acquired by using a 100 × objective lens (Nikon LU Plan Fluor) with a numerical aperture of 0.9. Changes in the chemical compositions at the sample surfaces were analyzed by using XPS (Ulvac-Phi PHI500, Japan) with Al Kα radiation. In particular, Ti 2p and O 1s peaks from the surfaces were used for the chemical composition analysis. The UV and visible-light absorption coefficients of samples were measured with UV-visible light absorption spectroscopy (Hitachi U-3900, Japan). Changes in the

electrical conductivities of samples were measured by using electrical impedance spectroscopy (Hioki 3522 LCR HiTESTER, Japan). The electrical conductivities in the presence and absence of light irradiation were especially compared because their difference was proportional to the photoexcited carrier concentration.

3. Results

3.1. UV- and visible-light-induced photodecomposition

Figure 1(a) shows the photodecomposition values of MB dye, $\ln(C/C_0)$, obtained under 365-nm UV irradiation for untreated and plasma-assisted-annealed P-25 NPs. The symbols C and C_0 are the MB dye concentrations at a given irradiation time and before UV irradiation, respectively. A small photodecomposition value of $\ln(C/C_0)$ signifies a high photodecomposition of MB dye. The photodecomposition values of the two samples decrease as the UV irradiation time lengthens. Comparing these values, the photodecomposition value of plasma-assisted-annealed P-25 NPs at an UV irradiation time of 4 h, −1.5, is approximately half that of untreated P-25 NPs, −0.76. In other words, the photodecomposition of plasma-assisted-annealed P-25 NPs is higher than that of untreated P-25 NPs. This indicates that the plasma-assisted annealing enhances the UV-induced photodecomposition of anatase/rutile-mixed phase TiO_2 NPs, as in the case of anatase phase TiO_2 NPs.[27] **Figure 1**(b) shows the photodecomposition values of P-25 NPs annealed in ambient air at a variety of temperatures. The photodecomposition values of air-annealed P-25 NPs are roughly similar to that of untreated P-25 NPs regardless of annealing temperature, except for that at 900 ℃, as opposed to the case of anatase phase TiO_2 NPs.[27] The air-annealing at 900 ℃ significantly deteriorates the original photodecomposition. The result indicates that the air annealing does not contribute to enhancing the photodecomposition of anatase/rutile-mixed phase TiO_2 NPs under UV irradiation. Thus, the plasma-assisted annealing is more effective and efficient than the

air-annealing for enhancing the UV-induced photodecomposition of anatase/rutile-mixed phase TiO_2 NPs.

The photodecomposition values of untreated and plasma-assisted-annealed P-25 NPs under 405-nm visible-light irradiation are compared as shown in **Figure 2**(a). There is also a clear difference in the photodecomposition value between these two samples. The photodecomposition value of plasma-assisted-annealed P-25 NPs at a visible-light irradiation time of 8 h, −0.8, is approximately three times smaller than that of untreated P-25 NPs, −0.3. This indicates that the plasma-assisted annealing enhances the visible-light-induced photodecomposition of anatase/rutile-mixed phase TiO_2 NPs, as in the case of UV irradiation. The photodecomposition values of P-25 NPs annealed in ambient air at a variety of temperatures are shown in **Figure 2**(b). The photodecomposition value of P-25 NPs annealed at 300 ℃ is similar to that of untreated P-25 NPs. The photodecomposition value of air-annealed P-25 NPs decreases as the annealing temperature rises to 700 ℃. Specifically, the photodecomposition value of 700 ℃-air-annealed sample at a visible-light irradiation time of 8 h, −0.6, is half that of untreated P-25 NPs, −0.3. However, the photodecomposition value increases with further increasing temperature from 700 to 900 ℃. For example, the photodecomposition value of 900 ℃-air-annealed sample at a visible-light irradiation time of 8 h, −0.2, is larger than that of untreated P-25 NPs, −0.3, suggesting the deterioration of the original photodecomposition. The comparison indicates that the photodecomposition induced under visible-light irradiation is more enhanced by the air annealing at 500−700 ℃, as opposed to the case of UV irradiation, but not higher than or not comparable to that exerted by the plasma-assisted annealing. Thus, the plasma-assisted annealing is also more effective even for enhancing the photodecomposition of anatase/rutile-mixed phase TiO_2 NPs under visible-light irradiation.

3.2. UV- and visible-light-induced photobactericidal efficacy

Figure 3 shows the log numbers of bacterial survival for untreated and plasma-assisted-annealed P-25 NPs in the presence of 365-nm UV irradiation. A small log number of bacterial survival signifies a high bactericidal efficacy. The log survival numbers of air-annealed P-25 NPs were not measured because the air-annealing does not enhance the photodecomposition (**Figure 1**(b)). The log survival numbers of air-annealed P-25 NPs are considered to be comparable to or larger than that of untreated P-25 NPs. The log survival number of untreated P-25 NPs reduces to 5 as the UV irradiation time lengthens to 2 min. For the plasma-assisted-annealed P-25 NPs, the reduction in the log survival number is larger; the UV irradiation for 2 min reduces the log survival number to 2. Specifically, the plasma-assisted-annealed P-25 NPs reduce the survival number by 4−5 orders of magnitude under UV irradiation for 2 min, and the untreated P-25 NPs reduce the survival number by 2 orders of magnitude. This indicates that the UV-induced bactericidal activity of plasma-assisted-annealed P-25 NPs is approximately 2 orders of magnitude greater than that of untreated P-25 NPs.

Figure 4 shows the log numbers of bacterial survival for untreated, plasma-assisted-annealed, and 700 ℃-air-annealed P-25 NPs in the presence of 405-nm visible-light irradiation. The log survival number of plasma-assisted-annealed P-25 NPs reduces to approximately 2 as the visible-light irradiation lengthens to 4 min. Specifically, the plasma-assisted-annealed P-25 NPs reduce the survival number by approximately 4 orders of magnitude under visible-light irradiation for 4 min. This reduction is the largest of the samples. The log survival number of air-annealed P-25 NPs is slightly smaller than or comparable to that of untreated P-25 NPs; they reduce the survival number by 2−3 orders of magnitude under visible-light irradiation for 4 min. The comparison suggests that the visible-light-induced bactericidal activity of plasma-assisted-annealed P-25 NPs is 1−2 orders magnitude greater than those of the other samples. Thus, the plasma-assisted

annealing is more effective for enhancing the UV- and visible-light-induced photobactericidal activities of anatase/rutile-mixed phase TiO_2 NPs.

In the absence of light irradiation, the log survival number of plasma-assisted-annealed P-25 NPs, 6.5, is comparable to the log survival number before light irradiation, 6.7; the other samples have a similar trend. This result suggests that the plasma-assisted-annealed anatase/rutile-mixed phase TiO_2 NPs have no bactericidal efficacy in the absence of light irradiation. This finding significantly differs from that of plasma-assisted-annealed anatase phase TiO_2 NPs that demonstrate a high bactericidal efficacy even in the absence of light irradiation.[27]

3.3. Surface morphologies, particle morphologies, and the crystal phase distributions

Figure 5 shows the comparison between SEM images of the surfaces of untreated, plasma-assisted-annealed, and air-annealed samples. Numerous aggregates composed of P-25 NPs are observed on the surfaces of all the samples. The number of P-25 NP aggregates with large sizes of more than 20 μm observed on the surface of plasma-assisted annealed sample is the smallest among the samples. This is also confirmed by comparing the RMS surface roughness values. The RMS surface roughness value of plasma-assisted annealed sample, 401 nm, is smaller than those of air-annealed and untreated samples, 487 nm and 1.127 μm, respectively. This indicates that the plasma-assisted annealing reduces the aggregate size of P-25 NP as in the case of ST-01 NPs.[27] When observing the sample surface at high magnification, a gathering of P-25 NP aggregates with various sizes does not appear, as opposed to the case of ST-01 NPs.[27] In other words, P-25 NPs immobilized on glass substrate are seen to be agglomerated with each other. This trend is observed in all the samples.

Figure 6 shows the comparison between the particle morphologies of untreated, plasma-assisted-annealed, and air-annealed samples. The size of plasma-assisted-

annealed particles is similar to that of untreated particles. In contrast, careful observation shows that the air-annealed sample contains the particles with larger sizes as reported in the literature.[26] However, the majority of air-annealed particles are seen to have a size similar to that of untreated particles. Thus, the plasma-assisted annealing does not change the particle size of P-25 NPs.

Figure 7 shows the comparison between the Raman spectra of untreated, plasma-assisted-annealed, and air-annealed samples. In the Raman spectra of untreated P-25 NPs, there are five peaks centered at approximately 150, 205, 407, 527, and 647 cm^{-1} due to the anatase phase.[36,37] These are symbolized by E_g (A), E_g (A), B_{1g} (A), A_{1g} (A), and E_g (A), respectively, where the symbol (A) signifies the anatase phase.[36,37] There are also other peaks centered at approximately 245, 458, and 622 cm^{-1} due to the rutile phase.[36,37] These peaks correspond to multi-photon process (R), E_g (R), and A_{1g} (R), respectively, where the symbol (R) signifies the rutile phase.[36,37] This result is consistent with that reported in the literature for P-25 NPs.[36,37] The Raman spectra of plasma-assisted-annealed P-25 NPs resemble those of untreated P-25 NPs. For the air-annealed P-25 NPs, a similar trend also appears; the Raman spectra of the three samples are similar. However, there is a difference between the crystal phase distributions of the samples as shown in **Figure 8**. This figure shows the Raman mapping images of the samples. The red portions correspond to the anatase-phase-related peak intensity at 130−160 cm^{-1}, and the green portions correspond to the rutile-phase-related peak intensity at 430−460 cm^{-1}. The green portions are seen to be randomly distributed in the Raman mapping image of untreated P-25 NPs. For the plasma-assisted-annealed P-25 NPs, a similar result is also observed. In contrast, the green portions are locally distributed in the Raman mapping image of air-annealed P-25 NPs. These results suggest that the air-annealing agglomerates the rutile phase particles, whereas the plasma-assisting annealing does not. On the other hand, the red portions in the Raman mapping images of the three samples are seen to be similar,

suggesting that the two post-treatment methods do not influence the distribution of anatase phase crystal. The difference may be attributed to the difference between the thermal conductivities of anatase and rutile phase crystals; the thermal conductivity of rutile phase crystal is larger than that of anatase phase crystal.[38] The rutile phase particles may be agglomerated via surface diffusion driven by 700 ℃-air-annealing, as in the case of Au thin films.[39] The formation of this agglomerate may also be related to the crystal instability of rutile phase particles with oxygen deficiency on the outmost surface due to 700 ℃-air-annealing.

3.4. Crystalline structures

Figure 9 shows the XRD patterns of untreated, plasma-assisted-annealed, and air-annealed P-25 NPs, which are superimposed on a halo pattern of the glass substrate. The XRD pattern of untreated P-25 NPs is composed of A(101), A(004), A(200), A(221) and A(105) plane orientations of anatase phase crystalline structure with lattice parameters, $a = b = 3.79$ Å and $c = 9.51$ Å[40] and of R(110) and R(101) plane orientations of rutile phase crystalline structure with lattice parameters, $a = b = 4.59$ Å and $c = 2.96$ Å.[41] Here, the symbols A and R signify the diffraction peaks of anatase and rutile phases, respectively. In the anatase phase, the intensity of A(101) diffraction peak is larger than those of other diffraction peaks, and in the rutile phase, the intensity of R(110) diffraction peak is larger. The XRD pattern of untreated P-25 NPs agrees with that reported in the literature.[42] The XRD pattern of plasma-assisted-annealed P-25 NPs roughly resembles that of untreated P-25 NPs, but the A(101) peak intensity appears to be slightly larger than that of untreated P-25. The XRD pattern of air-annealed P-25 NPs appears to be similar to that of untreated P-25 NPs.

However, a detailed analysis demonstrates a modification of crystal structure induced by the plasma-assisted annealing. **Figure 10** shows the comparison between the

anatase/rutile ratios of the samples. The anatase/rutile phase ratios are estimated from the equation, 0.8 I_A / I_R, where I_A and I_R are the intensities of A(101) and R(110) diffraction peaks, respectively.[43,44] These values of I_A and I_R are taken from the data in **Figure 9**. The plasma-assisted annealing increases the anatase/rutile phase ratio of P-25 NPs, indicating that the plasma-assisted annealing increases the density of anatase phase crystal or decreases the density of rutile phase crystal. This may be due to the amorphization or destruction of rutile phase TiO_2 structures originating from the plasma irradiation and/or due to the growth of anatase phase TiO_2 structures by repairing oxygen deficiency on the outermost surface with the plasma irradiation. The change in the anatase/rutile phase ratio induced by the plasma-assisted annealing significantly differs from that induced by the air-annealing. The air-annealing hardly changes or only slightly decreases the anatase/rutile phase ratio of P-25 NPs, indicating that the air-annealing increases the density of rutile phase crystal or decreases the density of anatase phase crystal. This is consistent with the result reported in the literature.[25] Thus, the plasma-assisted annealing facilitates the phase transformation to the anatase phase, as opposed to the air-annealing.

3.5. Chemical compositions

Figure 11 shows the O 1s and Ti 2p regions of measured XPS spectra of untreated, plasma-assisted-annealed, and air-annealed P-25 NPs. The O 1s spectrum of plasma-assisted-annealed P-25 NPs significantly differs from that of untreated P-25 NPs. The O 1s spectrum of plasma-assisted-annealed P-25 NPs has two distinct peaks at binding energies of approximately 530 and 532 eV. In contrast, the Ti 2p spectra of the two samples are the same, having Ti $2p_{3/2}$ at 457.8 eV and Ti $2p_{1/2}$ peaks at 463.5 eV due to the Ti−O bond.[45,46] For air-annealed P-25 NPs, the O 1s and Ti 2p spectra are considerably similar to those of untreated P-25 NPs, suggesting that the air-annealing

hardly influences the O 1s and Ti 2p spectra. Thus, the plasma-assisted-annealing influences only the O 1 spectrum of anatase/rutile-mixed phase TiO_2 NPs, as in the case of anatase phase TiO_2 NPs.[27]

The peak decomposition of the O 1s spectra into three pseudo-Voigt functions brings about a deep understanding of the compositional changes induced by the plasma-assisted annealing. The pseudo-Voigt functions used are located at binding energies of 529.7, 531.0, and 532.3 eV, which correspond to O−Ti bond in TiO_2 lattice, bridging oxygen groups, and terminal oxygen groups adsorbed on the surface, respectively.[47,48] The pseudo-Voigt functions are determined so that the curves for the sum of the three pseudo-Voigt functions (black curves) reproduce the measured O 1s spectra (red open circles) as shown in **Figures 11**(a)−(c). The O/Ti ratios of O−Ti bond, bridging oxygen groups, and terminal oxygen groups are estimated from multiplying the total O/Ti ratio by their fractions determined from the peak decomposition analysis, respectively, as shown in **Figure 12**. The total O/Ti ratio is the ratio of the integrated intensity of measured O 1s peak to the integrated intensity of measured Ti 2p peak. The plasma-assisted annealing reduces the O/Ti ratio of O−Ti bond but increases the O/Ti ratios of bridging and terminal oxygen groups. This indicates that the plasma-assisted annealing causes the lattice oxygen deficiency or oxygen vacancies and introduces more bridging and terminal oxygen groups. This compositional change of plasma-assisted-annealed P-25 NPs is roughly similar to that of plasma-assisted-annealed ST-01 NPs.[27] However, when compared in detail, the O/Ti ratios of O−Ti bond and bridging oxygen groups for plasma-assisted-annealed P-25 NPs are smaller than those of plasma-assisted-annealed ST-01 NPs. This implies that the plasma-assisted annealing neither causes the lattice oxygen deficiency nor increases the bridging oxygen groups in anatase/rutile-mixed phase TiO_2 NPs in comparison with those in anatase TiO_2 NPs. This difference may be related to the fact that, in the absence of light irradiation, the plasma-assisted-annealed anatase/rutile-mixed phase TiO_2 NPs have no

bactericidal efficacy, whereas the plasma-assisted-annealed anatase phase TiO_2 NPs have the bactericidal efficacy.[27] The air-annealing of P-25 NPs slightly reduces the O/Ti ratio of O−Ti bond and hardly influences the O/Ti ratios of bridging and terminal oxygen groups.

3.6. Optical absorptions

Figure 13(a) shows the comparison between the UV absorption coefficients of untreated and plasma-assisted-annealed P-25 NPs at a wavelength of 365 nm. The absorption coefficient of plasma-assisted-annealed P-25 NPs is larger than that of untreated P-25 NPs. The result indicates that the plasma-assisted annealing enhances the absorption of 365-nm UV in anatase/rutile-mixed phase TiO_2 NPs. This increasing trend of UV absorption is similar to that of anatase phase TiO_2 NPs annealed with the plasma.[27] Even in the case of 405-nm visible-light, a similar increasing trend is also observed as shown in **Figure 13**(b). The absorption coefficient of plasma-assisted-annealed P-25 NPs is the largest among the samples, indicating that the plasma-assisted annealing enhances the absorption of 405-nm visible-light in comparison with air-annealing. Thus, the plasma-assisted annealing contributes to the enhanced visible-light absorption as well as the enhanced UV absorption of anatase/rutile-mixed phase TiO_2 NPs.

3.7. Electrical conductivities

Figure 14(a) shows the comparison between the electrical conductivities of the samples in the presence and absence of 365-nm UV irradiation. In the absence of UV irradiation, the conductivity of plasma-assisted-annealed P-25 NPs is smaller than that of untreated P-25 NPs. This suggests that the plasma-assisted annealing contributes to reducing the concentration of residual charged carriers attributed to oxygen vacancies unintentionally present in TiO_2.[49,50] The oxygen vacancies are known to act as shallow

donors.[49−51] In the presence of UV irradiation, the conductivities of samples become larger because of UV-photoexcited carriers generated in the samples. In particular, the UV-induced conductivity of plasma-assisted-annealed P-25 is larger than that of untreated P-25 NPs. This difference is quantitatively confirmed in **Figure 14**(b). This figure shows the UV-induced relative conductivities, which are determined by a difference between the conductivities in the presence and absence of UV irradiation. The UV-induced relative conductivity of plasma-assisted-annealed P-25 NPs is larger than that of untreated P-25 NPs. This indicates that the plasma-assisted annealing contributes to increasing the concentration of UV-photoexcited carries in anatase/rutile-mixed phase TiO_2 NPs, as in the case of anatase phase TiO_2 NPs.[27] Even in the presence of 405-nm visible-light irradiation, the conductivity of plasma-assisted-annealed P-25 NPs is larger than those of the other samples or comparable to that of air-annealed sample as shown in **Figure 15**(a). In contrast, in the absence of visible-light irradiation, the conductivity of plasma-assisted annealed sample is the smallest among the samples. The visible-light-induced relative conductivity of plasma-assisted-annealed P-25 NPs is accordingly larger as shown in **Figure 15**(b). Thus, the plasma-assisted annealing is found to contribute not only to increasing the concentration of UV-photoexcited carriers but also to increasing the concentration of visible-light-photoexcited carriers in anatase/rutile-mixed phase TiO_2 NPs.

4. Discussion

The plasma-assisted-annealed P-25 NPs exhibit higher UV- and visible-light-induced photodecomposition and photobactericidal activities than the air-annealed P-25 NPs do, as shown in **Figures 1−4**. The enhanced UV- and visible-light photocatalytic activities of P-25 NPs due to the plasma-assisted annealing correlate closely with the increased UV- and visible-light-induced relative conductivities, respectively (**Figures 14** and **15**). This

suggests that the photoexcited carrier concentrations increased by the plasma-assisted annealing under UV and visible-light irradiations greatly contribute to the enhanced photocatalytic activities. The photoexcited carrier concentration increased under UV irradiation is discussed in terms of the following four factors observed: the facilitated phase transformation to anatase phase, the introduction of more oxygen vacancies, the increased amounts of bridging and terminal oxygen groups, and the reduced P-25 NP aggregate size. The first factor for the increased photoexcited carrier concentration is the phase transformation to the anatase phase induced by the plasma-assisted annealing (**Figure 10**). The anatase phase TiO_2 (101) surface has a substantially higher photocatalytic activity than the rutile phase TiO_2 (110) surface has.[52,53] This originates from a huge difference in the photoexcited carrier lifetime between anatase and rutile phase crystals. The photoexcited carrier lifetime for the anatase phase crystal (> 10 ns) is about an order of magnitude larger than that for the rutile phase crystal (< 1 ns).[52,53] This difference is based on the fact that the energy band structures of anatase and rutile phase crystals exhibit an indirect bandgap and a direct bandgap, respectively.[54,55] The direct bandgap structure of rutile phase crystal allows the photoexcited charge carriers to easily recombine each other with the emission of photons. In contrast, the indirect bandgap structure of anatase phase crystal allows the photoexcited charge carriers to recombine each other with the assistance of phonons. This assistance of phonons suggests that the photogenerated electrons in the anatase phase crystal do not directly recombine the photogenerated holes, extending the photoexcited carrier lifetime and increasing the photoexcited carrier concentration.[54,55] Thus, the phase transformation to the anatase phase would contribute to the enhanced photoexcited carrier concentration under UV irradiation.

The second factor for the increased photoexcited carrier concentrations is the introduction of more oxygen vacancies into the plasma-assisted-annealed sample **(Figure**

12(a)). The oxygen vacancies located at 0.75−1.18 eV below the conduction band edge are responsible for the long lifetime of the photoexcited carriers.[49−51,56] The introduction of more oxygen vacancies is also confirmed by comparing the temperature dependences of photoluminescence (PL) spectra from the samples as shown in **Figure 16**. The PL spectra were measured at various sample temperatures with an excitation light of 313 nm in wavelength (4 eV in photon energy). In the PL spectrum of untreated sample at a low temperature of 16.6 K, an emission peak appears around a photon energy of 2.3 eV. A similar trend also appears in the PL spectrum of plasma-assisted-annealed sample at 16.6 K. For the PL spectrum of air-annealed sample at 16.6 K, two emission peaks appear at photon energies of 1.5 and 2.3 eV. The 2.3 eV emission peak originates from radiative recombination of self-trapped excitons trapped by oxygen vacancies in TiO_2.[57−59] The 2.3 eV emission peak intensities of plasma-assisted-annealed and air-annealed samples are quite similar, and they are larger than that of untreated sample. This result indicates that the plasma-assisted annealing and air-annealing introduce a larger amount of oxygen vacancies into P-25 NPs. The 1.5 eV emission peak observed only for the air-annealed sample originates from titanium interstitial atoms or titanium vacancies.[57−59] This suggests that, in addition to oxygen vacancies, the air-annealing also introduces a larger amount of titanium interstitial atoms or titanium vacancies into P-25 NPs. The 2.3 eV emission peak intensities of untreated and air-annealed samples decrease while shifting to the higher-photon-energy side owing to strong lattice relaxation[59] as the temperature rises from 16.6 K to room temperature. This is termed thermal quenching.[60] In contrast, the 1.5 eV emission peak observed only in the air-annealed sample intensity increases as the temperature rises, then decreases and finally disappears at room temperature. This is termed negative thermal quenching, which frequently appears in a variety of semiconductors.[60] Ultimately, the PL spectra of untreated and air-annealed samples at room temperature become quite similar. In the case of plasma-assisted annealing, a

similar temperature dependence of 2.3 eV emission peak intensity also appears. However, the 2.3 eV emission peak intensity at room temperature is larger and shifts more significantly to the higher-photon-energy side, in comparison with the other samples. The larger shift of 2.3 eV emission peak to the higher-photon-energy side is consistent with the facilitated phase transformation to the anatase phase having a larger bandgap energy (**Figure 10**). Thus, the comparison between the PL spectra from the samples indicates that a larger amount of oxygen vacancies is present in the plasma-assisted-annealed sample even at room temperature. The introduction of such oxygen vacancies would be due predominantly to the impact of O_2^+, O_2^-, and O_3^- oxygen ions coming from the O_2 plasma onto the surface.[27] The larger amount of oxygen vacancies acts as more trapping sites of photoexcited electrons as schematically illustrated in the black-colored portions marked with (i) of **Figure 17**, reducing the recombination degree of more photoexcited carriers.[56] This would contribute to the enhanced photoexcited carrier concentration under UV irradiation.

The third factor for the increased photoexcited carrier concentration under UV irradiation is the increased amounts of bridging and terminal oxygen groups (**Figures 12**(b) and **12**(c)). In the O_2 plasma generated at atmospheric-pressure, there are large numbers of oxygen molecules and radicals such as O_2 and O. More oxygen molecules and radicals are preferentially adsorbed on more subsurface oxygen vacancies introduced, capturing or sharing excess electrons located on the oxygen vacancy sites.[61–64] As a result, this oxygen adsorption contributes to increasing the upward band-bending at the surface.[65] The oxygen adsorption also depresses the residual charged carrier concentration, reducing the electrical conductivity of the plasma-assisted-annealed sample **(Figures 14** and **15**). The depressed residual charged carrier concentration contributes to increasing the width of the depletion layer from the surface. This reason is that the depletion layer width is inversely proportional to the square root of charged carrier

concentration.[66,67] The increased upward band-bending and depletion layer width intensify the near-surface electric field that plays a crucial role in the separation of photoexcited carriers.[66,67] Specifically, the increased upward band-bending enhances the strength of the near-surface electric field, and the increased depletion layer width extends the region of the near-surface electric field, as schematically illustrated in the green-colored portions marked with (ii) of **Figure 17**. Furthermore, the intensified near-surface electric field can facilitate the charge transfer from rutile to anatase phase crystals.[68,69] The conduction band edge of rutile phase crystal is located at an energy of 0.2 eV above that of anatase phase crystal as drawn in **Figure 17** because the work function of rutile phase crystal is 0.2 eV lower than that of anatase phase crystal.[70] Considering this band alignment, the photogenerated electrons in the conduction band of rutile phase crystal can transfer to the conduction band of anatase phase crystal at an interface between the rutile and anatase phases. In contrast, the photogenerated holes cannot transfer from the rutile phase crystal. This can be accelerated by the intensified near-surface electric field, further enhancing the charge separation. Thus, the increased amounts of bridging and terminal oxygen groups can increase the upward band-bending, the depletion layer width at the surface, and the charge transfer from rutile to anatase phase crystals, facilitating the separation of photoexcited carriers. This would contribute to the enhanced photoexcited carrier concentration under UV irradiation.

The fourth factor for the increased UV-photoexcited carrier concentrations is the size reduction of P-25 NP aggregates (**Figure 5**). The size reduction of P-25 NP aggregates can enhance the scattering of incident light. This contributes to the increased optical absorption (**Figure 13**) as in the case of ST-01 NPs.[27] Thus, the reduced P-25 NP aggregates size would be relevant to the enhanced photoexcited carrier concentration under UV irradiation.

The increased photoexcited carrier concentration under visible-light irradiation is

attributed primarily to the introduction of more oxygen vacancies, the increased amounts of bridging and terminal oxygen groups, and the reduced TiO_2 NP aggregate size, as discussed in the case of UV irradiation. This is because these key factors are experimentally observed independently of polymorphs, i.e., anatase and rutile phases. However, in the case of visible-light irradiation, the increased charge separation and charge transfer of photoexcited carriers due to the above-mentioned key factors in the rutile phase crystal are considered to be responsible predominantly for the enhanced photocatalytic activities because of its smaller bandgap energy as drawn in **Figure 17**.

The higher UV- and visible-light-induced photodecomposition and photobactericidal activities induced by the plasma-assisted annealing would be attributed to more reactive oxygen species (ROS) produced by the increased bridging and terminal oxygen groups on the surface (**Figures 12**(b) and **12**(c)) due to the photoexcited carriers, as discussed in the literature.[27] In the plasma-assisted-annealed sample, more superoxide anion radicals, O_2^-, can be generated from the increased terminal oxygen groups due to the transfer of photogenerated electrons.[71] The generated O_2^- can be oxidized into singlet oxygen radicals, $^1O_2$, by photogenerated holes.[67] Moreover, these ROS can generate hydroxyl radicals through the photocatalytic reactions.[27,71] Thus, more ROS produced from the increased bridging and terminal oxygen groups due to the photoexcited carriers would also contribute to enhancing the UV- and visible-light-induced photodecomposition and photobactericidal activities.

5. Conclusion

We have clarified the photocatalytic activities of anatase/rutile-mixed phase TiO_2 NPs annealed with low-temperature O_2 plasma, by comparing them with those of air-annealed samples. Under not only 365-nm UV irradiation but also 405-nm visible-light irradiation, the photocatalytic activities of plasma-assisted-annealed sample greatly enhance as

compared with the untreated sample. The photocatalytic activities of air-annealed samples vary depending on the wavelength of the light-source. The photocatalytic activities of samples annealed in ambient air at various temperatures do not enhance under 365-nm UV irradiation. In contrast, the photocatalytic activities of samples annealed in ambient air at 500−700 °C greatly enhance as compared with that of the untreated sample under 405-nm visible-light irradiation, but do not enhance as much as those of the plasma-assisted-annealed sample. The plasma-assisted-annealing facilitates the phase transformation to anatase phase in TiO_2 NPs, introduces more oxygen vacancies in the surface, increases the amounts of bridging/terminal oxygen groups adsorbed on the surface, and reduces the size of TiO_2 NP aggregates formed on the surface. The enhanced photocatalytic activities due to the plasma-assisted annealing are attributed to the increased photoexcited carrier concentrations under UV irradiation and visible-light irradiation. The increased photoexcited carrier concentrations would be discussed in terms of the four key factors observed: the facilitated phase transformation to anatase phase (a), the introduction of more oxygen vacancies (b), the increased amounts of bridging/terminal oxygen groups (c), and the reduced TiO_2 NP aggregate size (d). The facilitated phase transformation to anatase phase (a) contributes directly to extending the photoexcited carrier lifetime. The introduction of more oxygen vacancies (b) contributes to trapping more photoexcited electrons. The increased amounts of bridging/terminal oxygen groups (c) contribute to increasing the upward band-bending at the surface, the depletion layer width from the surface, and the charge transfer from rutile to anatase phases. These two key factors, (b) and (c), facilitate the separation of photoexcited carriers, extending the photoexcited carrier lifetime. The reduced TiO_2 NP aggregate size (d) contributes to increasing the amounts of UV and visible-light optical absorptions. More ROS produced from the increased bridging/terminal oxygen groups by the photoexcited carriers would also enhance the UV- and visible-light-induced

photodecomposition and photobactericidal activities. The present findings are extremely important for deeply understanding the photocatalysis of anatase/rutile-mixed phase TiO_2 NPs. The plasma-assisted annealing will provide a new perspective on further improving the photocatalytic activities of anatase/rutile-mixed phase TiO_2 NPs under not only UV irradiation but also visible-light irradiation.

Acknowledgments

Part of this work was supported by JSPS KAKENHI Grant Number 20K03917.

Conflict of Interest

The authors declare no conflict of interest.

Data Availability Statement

The data that support the findings of this study are available from the corresponding author upon reasonable request.

References

[1] J. J. R. Marquez, I. Levchuk, P. F. Ibanez, M. Sillanpaa, *J. Clean. Prod.* **2020**, *258*, 120694.

[2] I. C. Ossai, A. Ahmed, A. Hassan, F. S. Hamid, *Environ. Technol. Inno.* **2020**, *17*, 100526.

[3] M. N. Subramaniam, P. S. Goh, W. J. Lau, A. F. Ismail, M. Karaman, *Powder Technol.* **2020**, *366*, 96.

[4] D. Komaraiah, E. Radha, J. Sivakumar, M. V. R. Reddy, R. Sayanna, *Opt. Mater.* **2020**, *108*, 110401.

[5] T. L. Tan, K. M. Lee, C. W. Lai, S. L. Hong, S. A. Rashid, *Adv. Powder Technol.* **2020**, *31*, 533.

[6] M. Abidi, A. Jajjaji, A. Bouzaza, K. Trablesi, H. Makhlouf, S. Rtimi, A. A. Assadi, *J. Photochem. Photobiol. A* **2020**, *400*, 112722.

[7] S. Chavan, V. Sarangdhar, V. Nadanathangam, *Emerg. Contam.* **2020**, *6*, 87.

[8] Y. Xu, X. Liu, Y. Zheng, C. Li, K. W. K. Yeung, Z. Cui, Y. Liang, Z. Li, S. Zhu, S. Wu, *Bioact. Mater.* **2021**, *6*, 1575.

[9] S. Lu, G. Meng, C. Wang, H. Chen, *Chem. Eng. J.* **2021**, *404*, 126526.

[10] H. Baniamerian, P. Tsapekos, M. A. Morales, S. Shokrollahzadeh, M. h Safavi, I. Angelidaki, *Inorg. Chem. Commun.* **2020**, *116*, 107936.

[11] D. Tekin, D. Birhan, H. Kiziltas, *Mater. Chem. Phys.* **2020**, *251*, 123067.

[12] A. G. Roman, C. Z. Islas, E. Q. Gonzalez, *Ceram. Int.* **2020**, *46*, 1137.

[13] X. Yang, Y. Song, T. Cao, L. Wang, H. Song, W. Lin, *Mol. Catal.* **2020**, *492*, 110971.

[14] A. Kaiba, O. Ouerghi, M. H. Geesi, A. Elsanousi, A. Belkacem, O. Dehbi, A. I. Alharthi, M. A. Alotaibi, Y. Riadi, *J. Mol. Struct.* **2020**, *1203*, 127376.

[15] A. Houas, H. Lachheb, M. Ksibi, E. Elaloui, C. Guillard, J. M. Herrmann, *Appl. Catal. B Environ.* **2001**, *31*, 145.

[16] M. Cho, H. Chung, W. Choi, J. Yoon, *Water Res.* **2004**, *38*, 1069.

[17] K. Ozawa, M. Emori, S. Yamamoto, R. Yukawa, S. Yamamoto, R. Hobara, K. Fujikawa, H. Sakama, I. Matsuda, *J. Phys. Chem. Lett.* **2014**, *5*, 1953.

[18] J. H. Huang, M. S. Wong, *Thin Solid Films* **2011**, *520*, 1379.

[19] L. Hou, M. Z. Zhongjie, Q. Li, J. Yang, *Appl. Surf. Sci.* **2018**, *428*, 640.

[20] Y. Ammari, K. E. Atmani, L. Bay, I. Bakas, S. Qourzal, I. A. Ichou, *Mater. Today: Proc.* **2020**, *22*, 126.

[21] D. A. Giannakoudakis, N. Farahmand, D. Lomot, K. Sobczak, T. J. Bandosz, J. C. Colmenares, *Chem. Eng. J.* **2020**, *395*, 125099.

[22] Y. Zhao, Y. Chi, C. Tian, Y. Liu, H. Li, A. Wang, *Water Res.* **2020**, *177*, 115789.

[23] L. A. A. Hajji, A. A. Ismail, A. A. Hazza, S. A. Ahmed, M. Alsaidi, F. Almutawa, A. Bumajdad, *J. Mol. Struct.* **2020**, *1200*, 127153.

[24] K. Priyanka, N. Remya, M. Behera, *J. Clean. Prod.* **2019**, *235*, 1.

[25] V. G. Bessergenev, M. C. Mateus, A. M. B. do Rego, M. Hantusch, E. Burkel, *Appl. Catal. A Gen.* **2015**, *500*, 45.

[26] T. Ishigaki, Y. Nakada, N. Tarutani, T. Uchikoshi, Y. Tsujimoto, M. Isobe, H. Ogata, C. Zhang, D. Hao, *R. Soc. Open Sci.* **2019**, *7*, 191539.

[27] R. Kawakami, Y. Yoshitani, A. Shirai, S. Yanagiya, H. Koide, Y. Mimoto, K. Kajikawa, M. Niibe, Y. Nakano, C. Azuma, T. Mukai, *Appl. Surf. Sci.* **2020**, *526*, 1466884.

[28] R. Kawakami, M. Niibe, Y. Nakano, Y. Araki, Y. Yoshitani, C. Azuma, T. Mukai, *Vacuum* **2018**, *152*, 265.

[29] A. Hassen, M. Mahrouk, H. Quzari, M. Cherif, A. Boudabous, J. J. Damelincourt, *Bioresour. Technol.* **2000**, *74*, 141.

[30] R. Kawakami, T. Inaoka, S. Minamoto, Y. Kikuhara, *Thin Solid Films* **2008**, *516*, 3478.

[31] Y. Ammari, K. E. Atmani, L. Bay, I. Backas, S. Qourzal, I. A. Ichou, *Mater. Today*

Proc. **2020**, *22*, 126.

[32] L. M. F. Arias, A. A. Duran, D. Cardona, E. Camps, M. E. Gomez, G. Zambrano, *J. Phys. Conf. Ser.* **2015**, *614*, 012008.

[33] A. Suligoj, U. L. Stangar, A. Ristic, M. Mazaj, D. Verhovsek, N. N. Tusar, *Appl. Catal. B: Environ.* **2016**, *184*, 119.

[34] Y. H. Joe, W. Ju, J. H. An, J. Hwang, *Aerosol Air Qual. Res.* **2014**, *14*, 928.

[35] S. Saitoh, K. Iwasaki, O. Yagi, *Microbes Environ.* **2003**, *18*, 210.

[36] J. Shen, H. Wang, Y. Zhou, N. Ye, G. Li, L. Wang, *RSC Adv.* **2012**, *2*, 9173.

[37] S. Challagulla, K. Tarafder, R. Ganesan, S. Roy, *Sci. Rep.* **2017**, *7*, 8783.

[38] X. Mettan, J. Jacimovic, O. S. Barisic, A. Pisoni, I. Batistic, E. Horvath, S. Brown, L. Rossi, P. Szirmai, B. Farkas, H. Berger, L. Forro, *Commun. Phys.* **2019**, *2*, 123.

[39] A. Herz, A. Franz, F. Theska, M. Hentschel, Th. Kups, D. Wang, P. Schaaf, *AIP Adv.* **2016**, *6*, 035109.

[40] H. Berger, H. Tang, F. Levy, *J. Cryst. Growth* **1993**, *130*, 108.

[41] A. V. Bandura J. D. Kubicki, *J. Phys. Chem. B* **2003**, *107*, 11072.

[42] M. Shaban, J. Poostforooshan, A. P. Weber, *J. Mater. Chem. A* **2017**, *5*, 18651.

[43] S. Saravanan, M. Balamurugan, T. Soga, *Trans. Mat. Res. Soc. Jpn.* **2018**, *43*, 255.

[44] R. A. Spurr, H. Myers, *Anal. Chem.* **1957**, *29*, 760.

[45] J. Lu, K. Liang, C. Xu, X. Wang, H. Ouyang, J. Huang, L. Feng, *Vacuum* **2019**, *163*, 292.

[46] P. Bindra, A. Hazra, *Vacuum* **2018**, *152*, 78.

[47] T. Kasuga, H. Kondo, M. Nogami, *J. Cryst. Growth* **2002**, *235*, 235.

[48] C. Y. Wu, K. J. Tu, J. P. Deng, Y. S. Lo, C. H. Wu, *Materials* **2017**, *10*, 566.

[49] Y. Chen, X. Luo, Y. Luo, P. Xu, J. He, L. Jiang, J. Li, Z. Yan, J. Wang, *Nanomaterials* **2019**, *9*, 698.

[50] Y. Wang, D. J. Doren, *Solid State Commun.* **2005**, *136*, 186.

[51] T. V. Perevalov, V. A. Gritsenko, *J. Exp. Theor. Phys.* **2011**, *112*, 310.

[52] T. Luttrell, S. Halpegamage, J. Tao, A. Kramer, E. Sutter, M. Batzill, *Sci. Rep.* **2014**, *4*, 4043.

[53] M. Xu, Y. Gao, E. M. Moreno, M. Kunst, M. Muhler, Y. Wang, H. Idriss, C. Woll, Phys. Rev. Lett. **2011**, *106*, 138301.

[54] J. Zhang, P. Zhou, J. Liu, J. Yu, *Phys. Chem. Chem. Phys.* **2014**, *16*, 20382.

[55] K. Ozawa, S. Yamamoto, K. Mase, I. Matsuda, *e-J. Surf. Sci. Nanotech.* **2019**, *17*, 130.

[56] B. Choudhury, A. Choudhury, *Physica E* **2014**, *56*, 364.

[57] S. A. Abdullah, M. Z. Sahdan, N. Nafarizal, H. Saim, A. S. Bakri, C. H. C. Rohaida, F. Adriyanto, Y, Sari, *J. Phys.: Conf. Ser.* **2018**, *995*, 012067.

[58] K. Wakabayashi, Y. Yamaguchi, T. Sekiya, S. Kurita, *J. Lumin.* **2005**, *112*, 50.

[59] M. L. Crespillo, J. T. Graham, F. Agulló-López, Y. Zhang, W. J. Weber, *Crystals* **2019**, *9*, 95.

[60] T. Wu, S. Jiang, P. N. Samanta, Y. Xie, J. Li, X. Wang, M. Devashis, X. Gu, Y. Wang, W. Huang, Q. Zhang, J. Leszczynski, D. Wu, *Chem. Comm.* **2020**, *56*, 12057.

[61] F. Guillemot, M. C. Porte, C. Labrugere, C. Baquey, *J. Colloid. Interf. Sci.* **2002**, *255*, 75.

[62] X. Pan, M. Q. Yang, X. Fu, N. Zhang, Y. J. Xu, *Nanoscale* **2013**, *5*, 3601.

[63] M. Setvin, U. Aschauer, P. Scheiber, Y. F. Li, W. Hou, M. Schmid, A. Selloni, U. Diebold, *Science* **2013**, *341*, 988.

[64] J. Gao, J. Lyu, J. Li, J. Shao, Y. Wang, W. Ding, R. Cheng, S. Wang, Z. He, *Langmuir* **2018**, *34*, 7034.

[65] S. Ma, M. E. Reish, Z. Zhang, I. Harrison, J. T. Tates, *J. Phys. Chem. C* **2017**, *121*, 1263.

[66] Z. Zhang, J. T. Yates, *Chem. Rev.* **2012**, *112*, 5520.

[67] L. Sang, Y. Zhang, J. Wang, Y. Zhao, Y. T. Chen, *Phys. Chem. Chem. Phys.* **2016**, *18*, 15427.

[68] D. C. Hurum, A. G. Agrios, K. A. Gray, T. Rajh, M. C. Thurnauer, *J. Phys. Chem. B* **2003**, *107*, 4545.

[69] A. Li, Z. Wang, H. Yin, S. Wang, P. Yan, B. Huang, X. Wang, R. Li, X. Zong, H. Han, C. Li, *Chem. Sci.* **2016**, *7*, 6076.

[70] D. O. Scanlon, C. W. Dunnill, J. Buckeridge, S. A. Shevlin, A. J. Logsdail, S. M. Woodley, C. R. A. Catlow, M. J. Powell, R. G. Palgrave, I. P. Parkin, G. W. Watson, T. W. Keal, P. Sherwood, A. Walsh, A. A. Sokol, *Nat. Mater.* **2013**, *12*, 798.

[71] Q. Chen, H. Wang, C. Wang, R. Guan, R. Duan, Y. Fang, X. Hu, *Appl. Catal. B Environ.* **2020**, *262,* 118258.

Figure captions:

Figure 1. 365-nm UV-induced photodecomposition values of MB dye, $\ln(C/C_0)$, as a function of irradiation time (a) for untreated and plasma-assisted-annealed P-25 NPs and (b) for P-25 NPs annealed in ambient air at a variety of temperatures.

Figure 2. 405-nm visible-light-induced photodecomposition values of MB dye, $\ln(C/C_0)$, as a function of irradiation time (a) for untreated and plasma-assisted-annealed P-25 NPs and (b) for P-25 NPs annealed in ambient air at a variety of temperatures.

Figure 3. The log numbers of bacterial survival for untreated and plasma-assisted-annealed P-25 NPs in the presence of 365-nm UV irradiation for 0, 1, and 2 min.

Figure 4. The log numbers of bacterial survival for untreated, plasma-assisted-annealed, and 700 ℃-air-annealed P-25 NPs in the presence of 405-nm visible-light irradiation for 0, 2, and 4 min.

Figure 5. SEM images of the surfaces of (a) untreated, (b) plasma-assisted-annealed, and (c) 700 ℃-air-annealed P-25 NPs.

Figure 6. Particle morphologies of (a) untreated, (b) plasma-assisted-annealed, and (c) 700 ℃-air-annealed P-25 NPs.

Figure 7. Raman spectra of (a) untreated, (b) plasma-assisted-annealed, and (c) 700 ℃-air-annealed P-25 NPs. The red and green curves were measured from the anatase-rich and the rutile-rich surface portions, respectively. The symbols (A) and (R) correspond to the peaks of anatase and rutile phases, respectively.

Figure 8. Raman mapping images of (a) untreated, (b) plasma-assisted-annealed, and (c) 700 ℃-air-annealed P-25 NPs. The red and green portions correspond to the anatase- and rutile-phase-related Raman peak intensities at 130−160 cm^{-1} and 430−460 cm^{-1}, respectively.

Figure 9. XRD patterns of untreated, plasma-assisted-annealed, and 700 ℃ air-annealed P-25 NPs. The symbols A and R represent the peaks of anatase and rutile phases, respectively.

Figure 10. Anatase/rutile phase ratios of untreated, plasma-assisted-annealed, and 700 ℃ air-annealed P-25 NPs.

Figure 11. O 1s regions in XPS spectra of (a) untreated, (b) plasma-assisted-annealed, and (c) 700 ℃-air-annealed P-25 NPs. (d) Ti 2p regions in XPS spectra of these samples.

Figure 12. O/Ti ratios of (a) O−Ti bond, (b) bridging oxygen groups, and (c) terminal oxygen groups for untreated, plasma-assisted-annealed, and 700 ℃-air-annealed P-25 NPs.

Figure 13. (a) Absorption coefficients of untreated and plasma-assisted-annealed P-25 NPs at a wavelength of 365 nm. (b) Absorption coefficients of untreated, plasma-assisted-annealed, and 700 ℃-air-annealed P-25 NPs at a wavelength of 405 nm.

Figure 14. (a) Electrical conductivities of untreated and plasma-assisted-annealed P-25 NPs in the presence and absence of 365-nm UV irradiation. (b) UV-induced relative

electrical conductivities of the samples.

Figure 15. (a) Electrical conductivities of untreated, plasma-assisted-annealed, and 700 ℃-air-annealed P-25 NPs in the presence and absence of 405-nm visible-light irradiation. (b) Visible-light-induced relative electrical conductivities of the samples.

Figure 16. Temperature dependences of PL spectra from (a) untreated, (b) plasma-assisted-annealed, and (c) 700 ℃-air-annealed P-25 NPs.

Figure 17. A proposed energy band structure model of anatase/rutile-mixed phase TiO_2 NPs annealed with O_2 plasma.

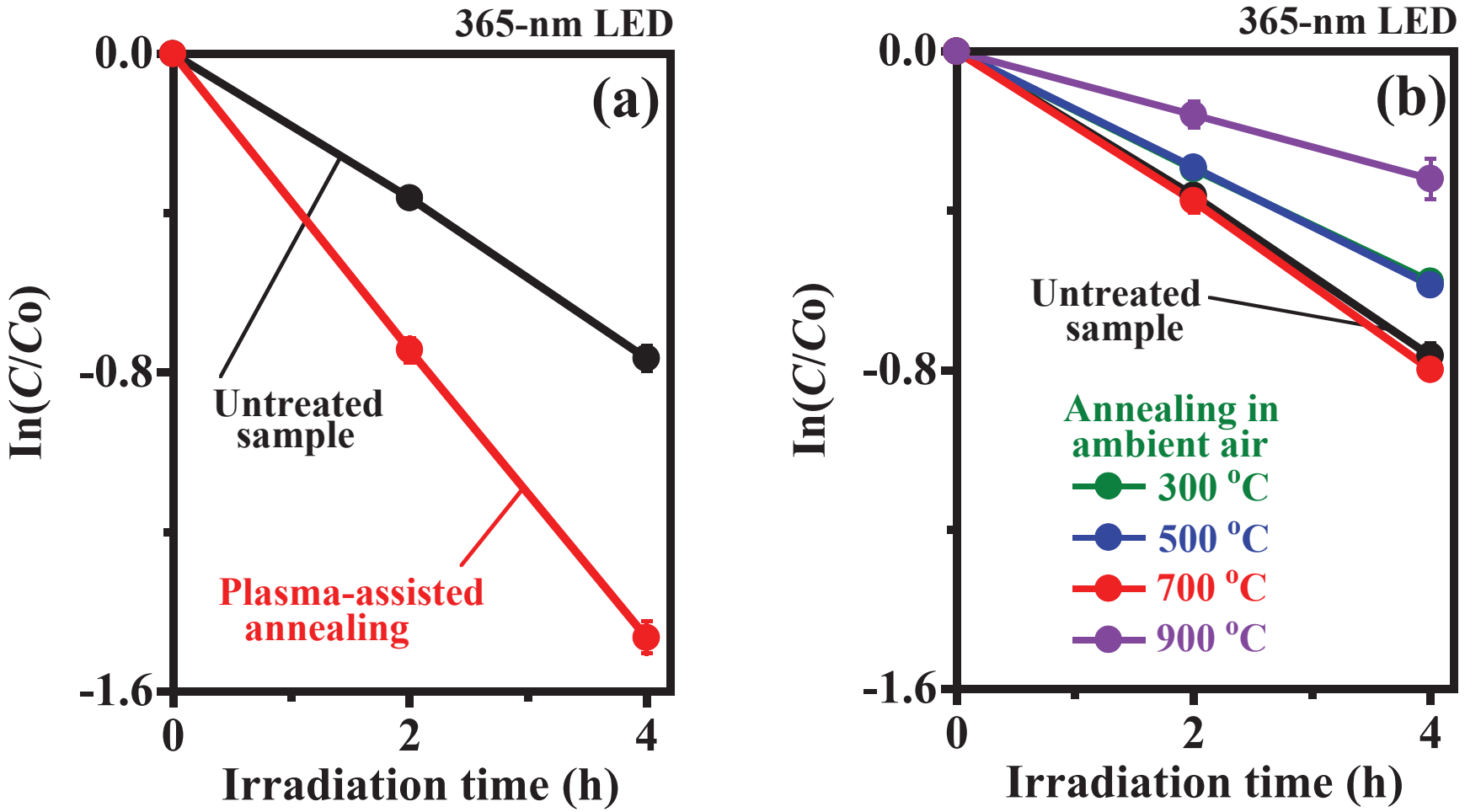

Figure 1. R. Kawakami *et al.*

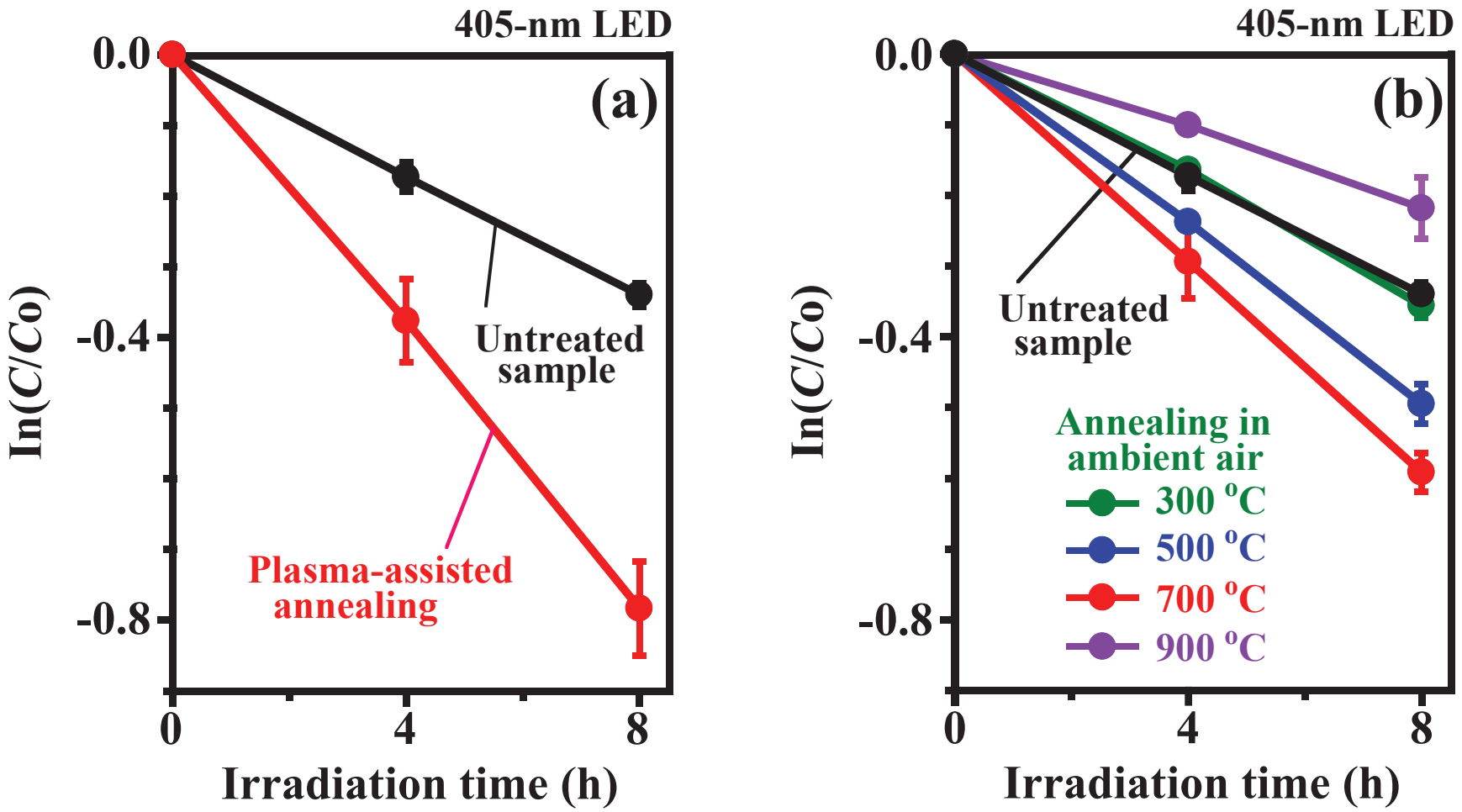

Figure 2. R. Kawakami *et al.*

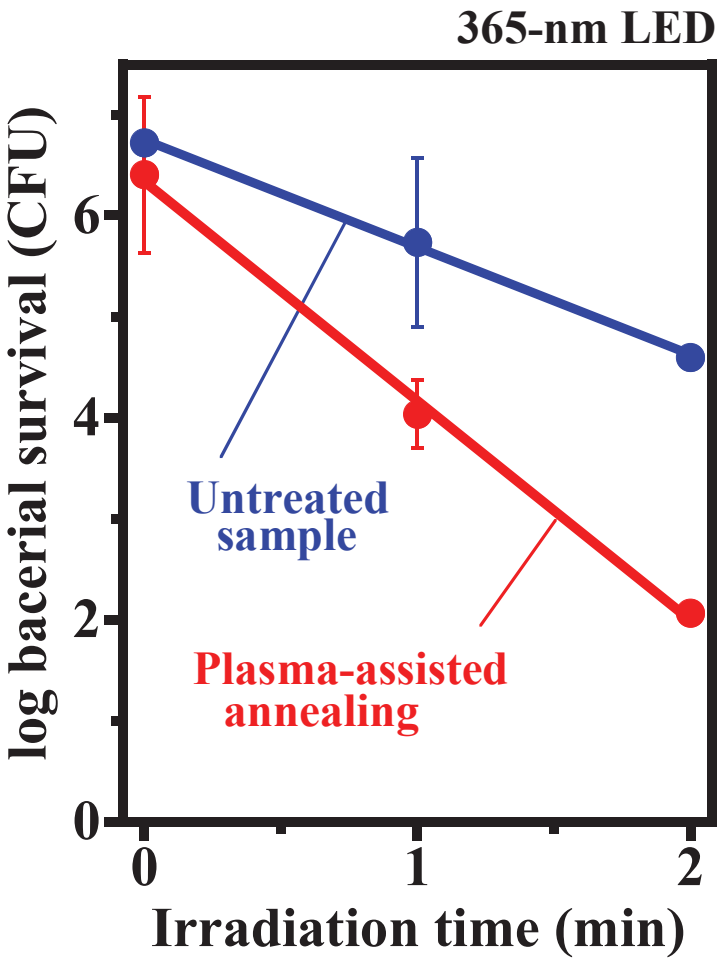

Figure 3. R. Kawakami *et al*.

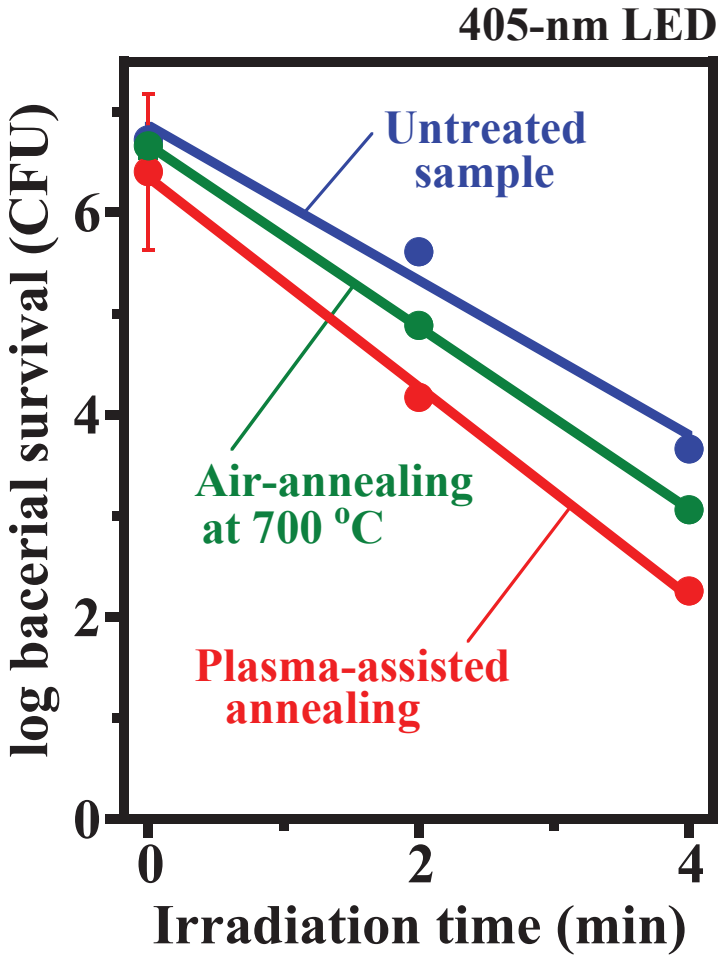

Figure 4. R. Kawakami *et al.*

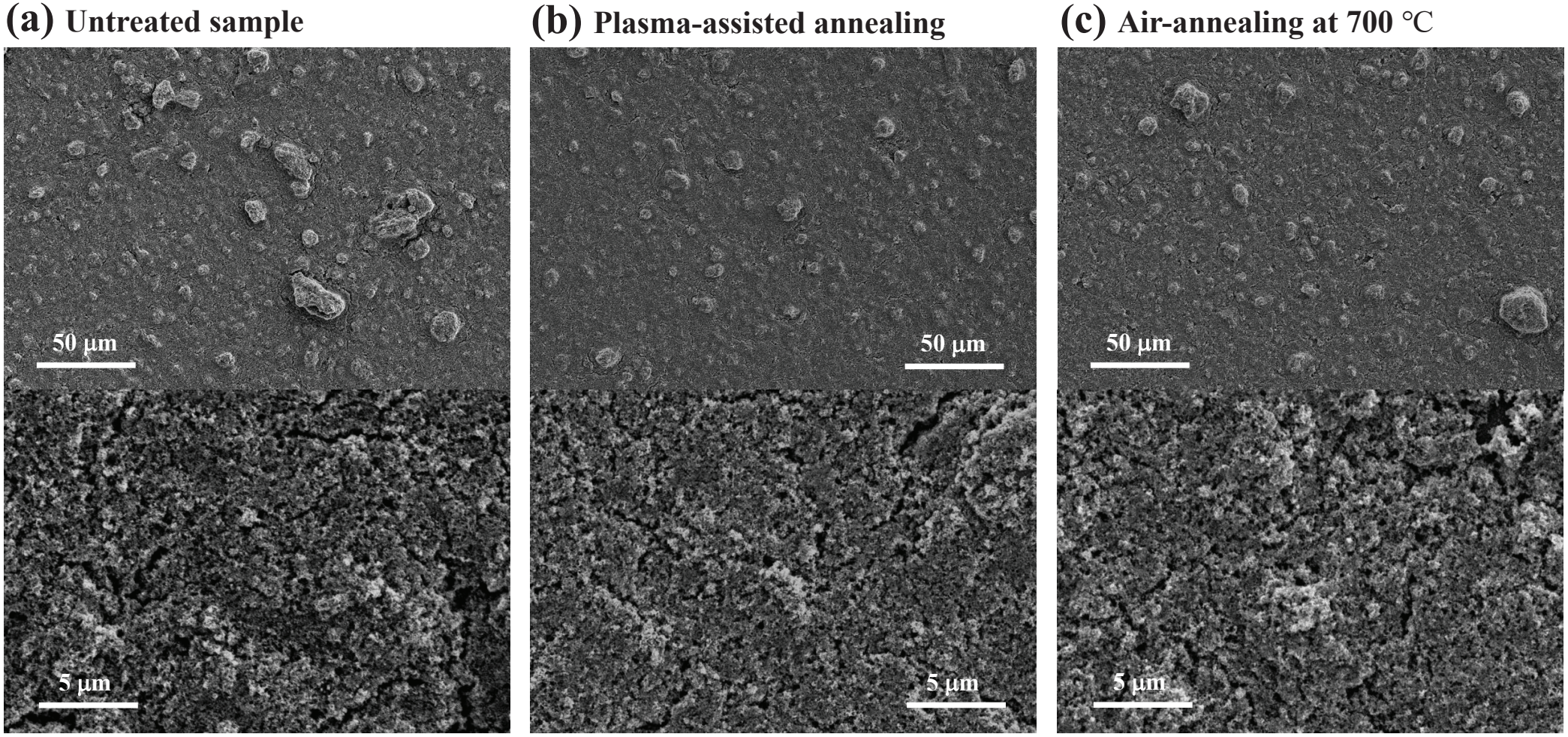

Figure 5. R. Kawakami *et al*.

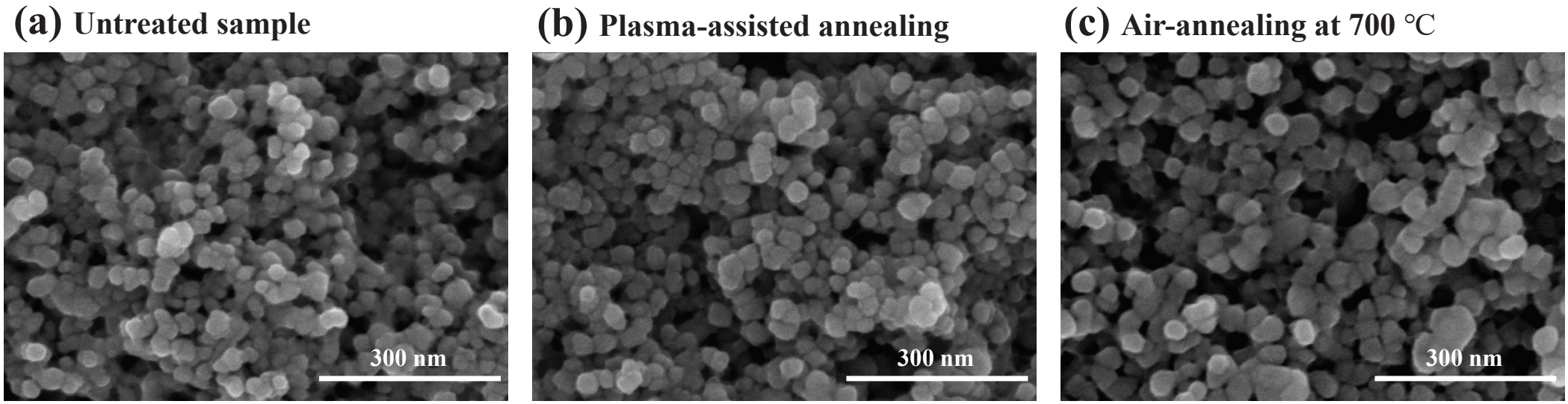

Figure 6. R. Kawakami *et al*.

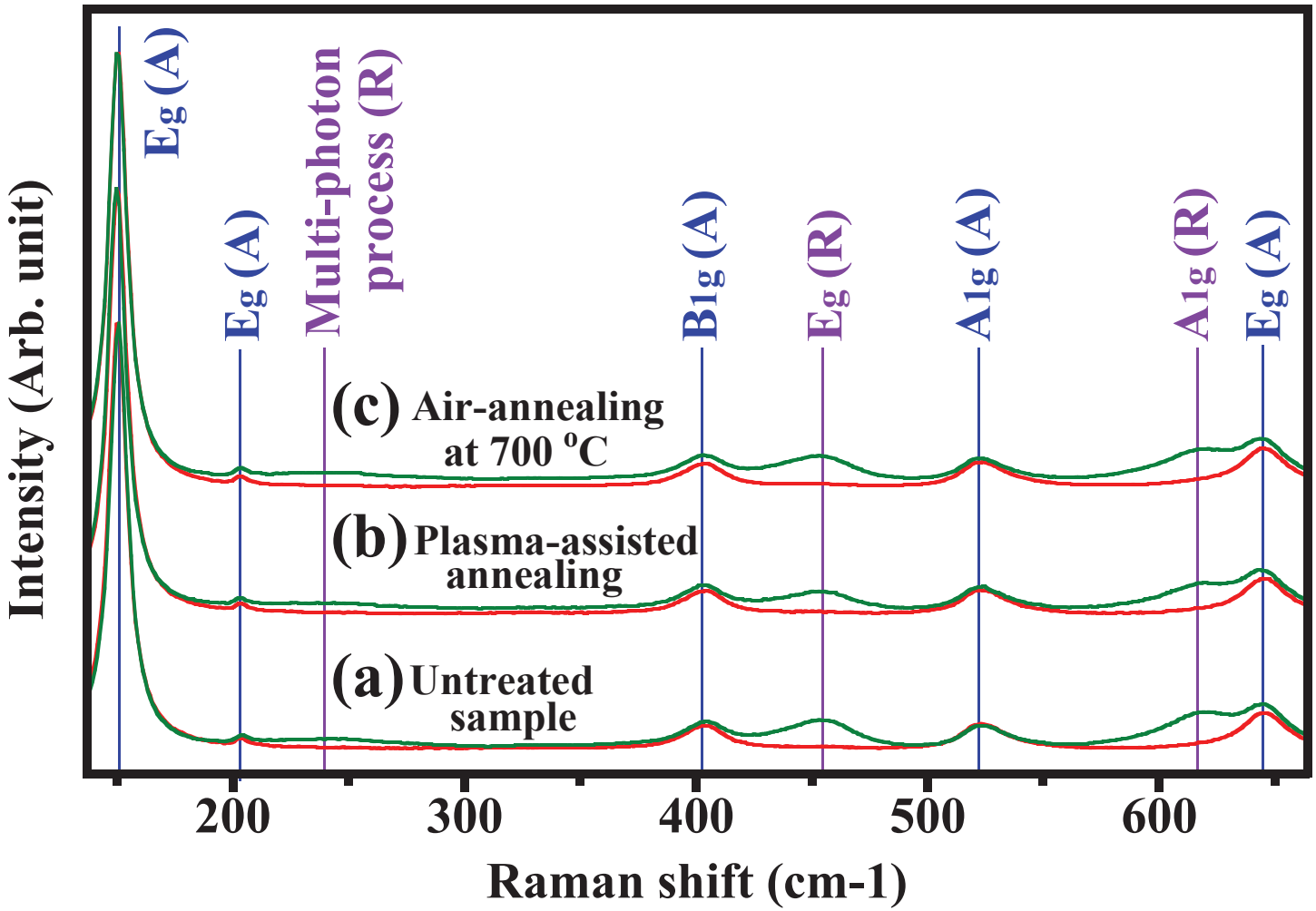

Figure 7. R. Kawakami *et al*.

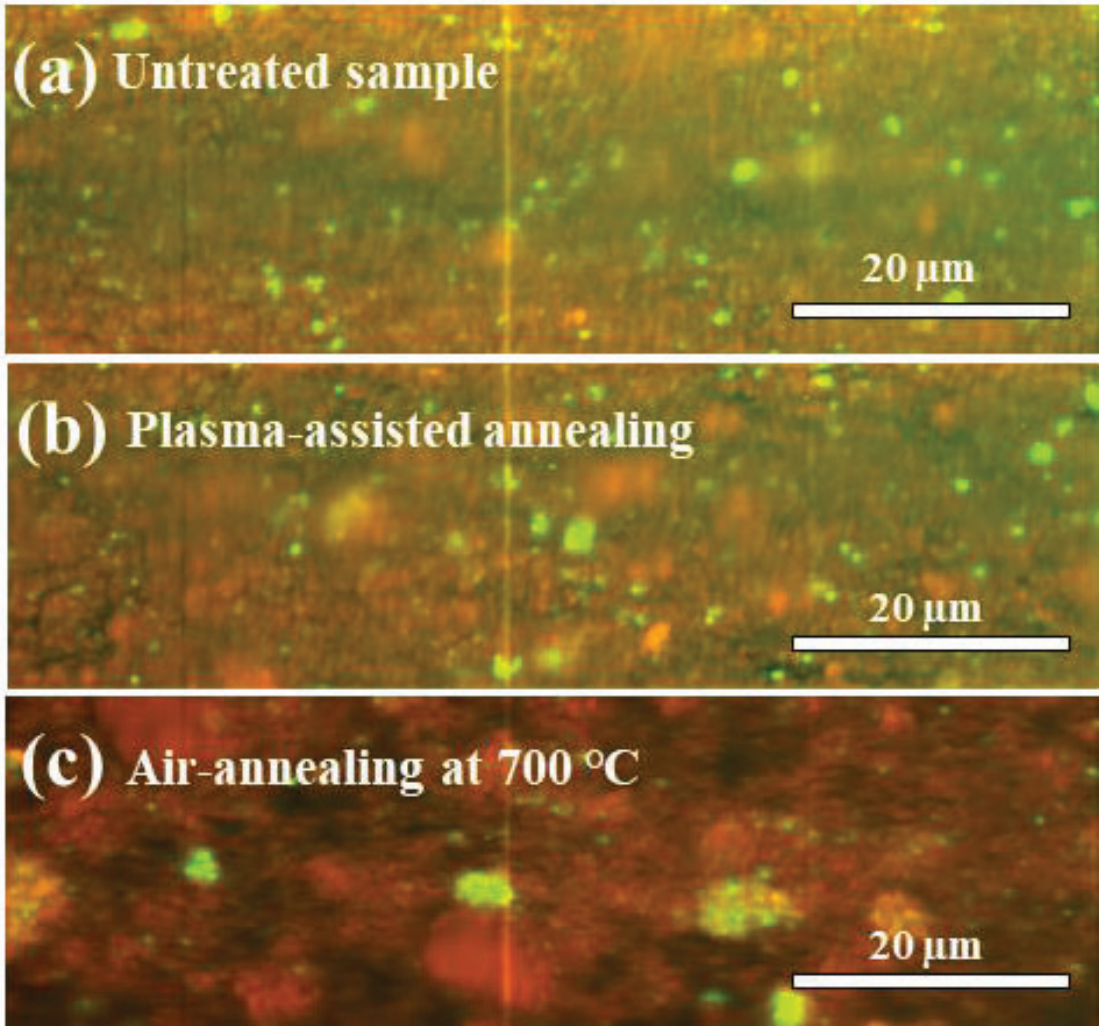

Figure 8. R. Kawakami *et al*.

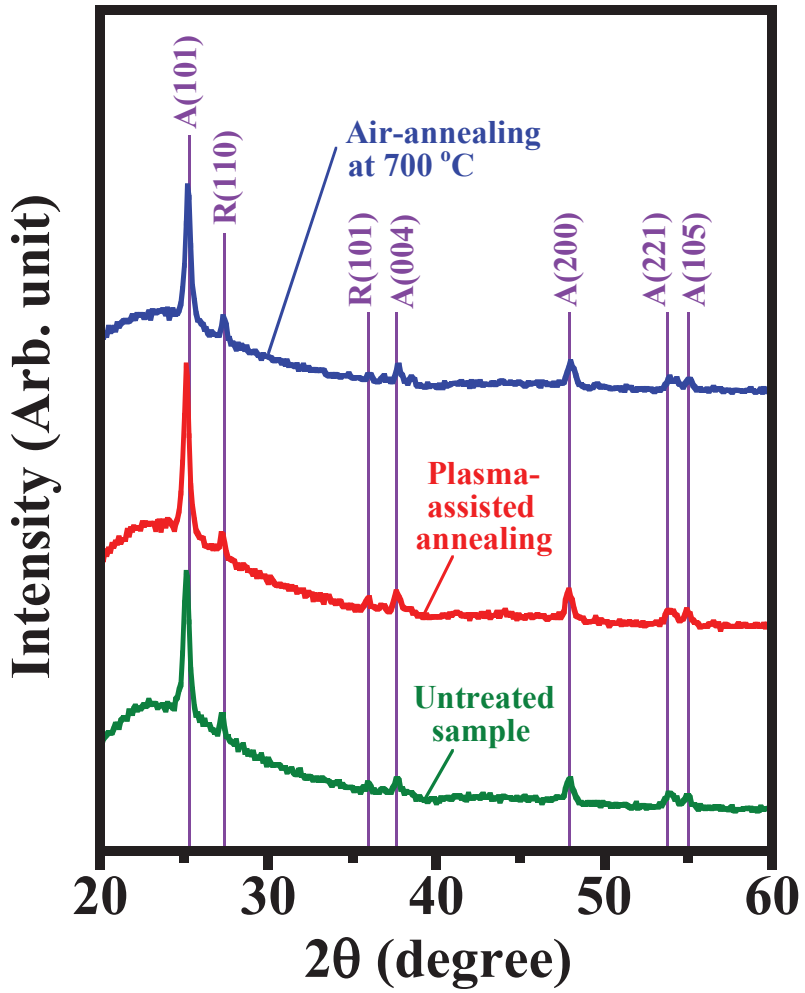

Figure 9. R. Kawakami *et al*.

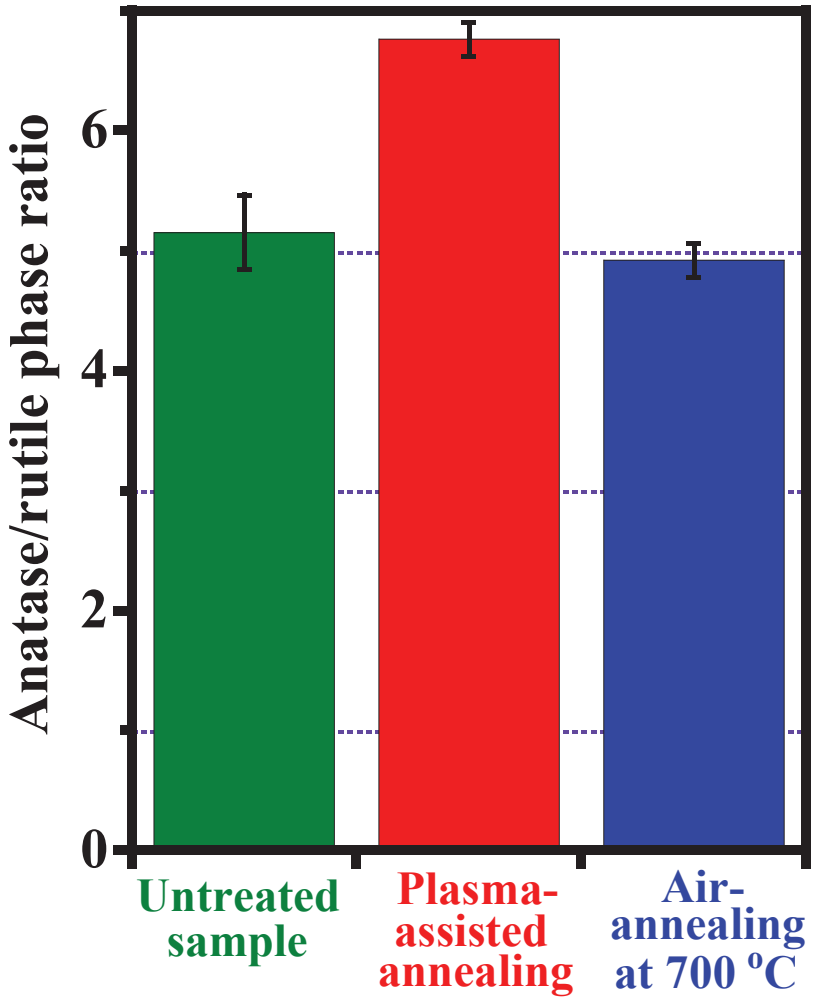

Figure 10. R. Kawakami *et al*.

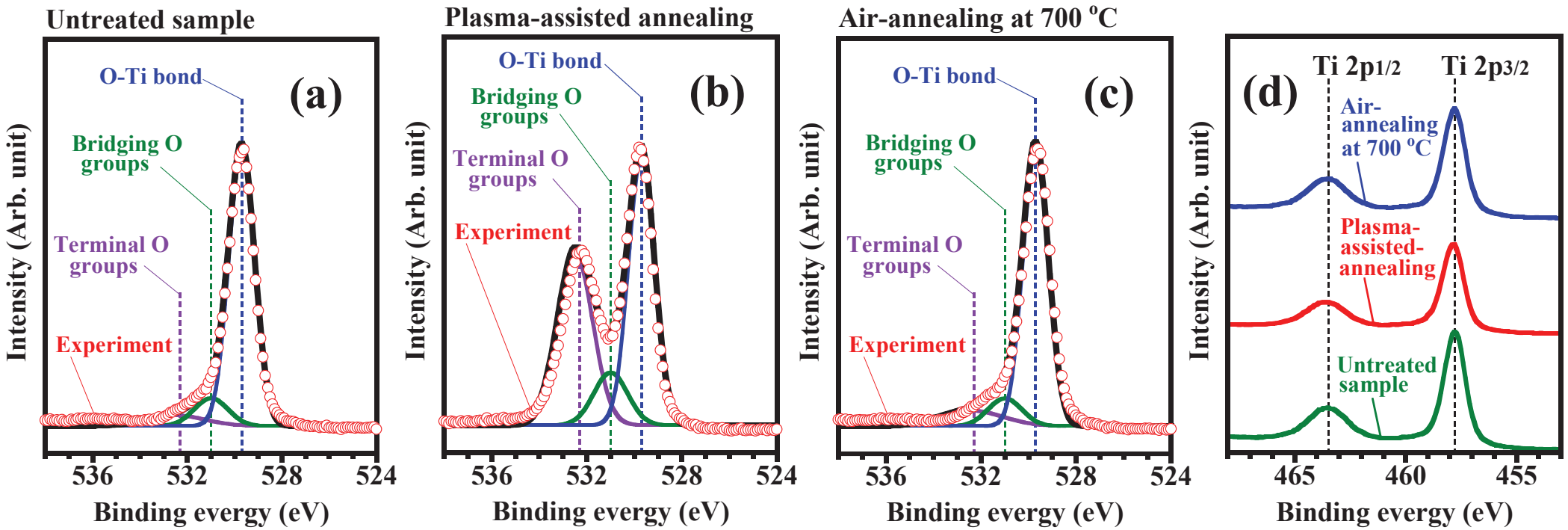

Figure 11. R. Kawakami *et al.*

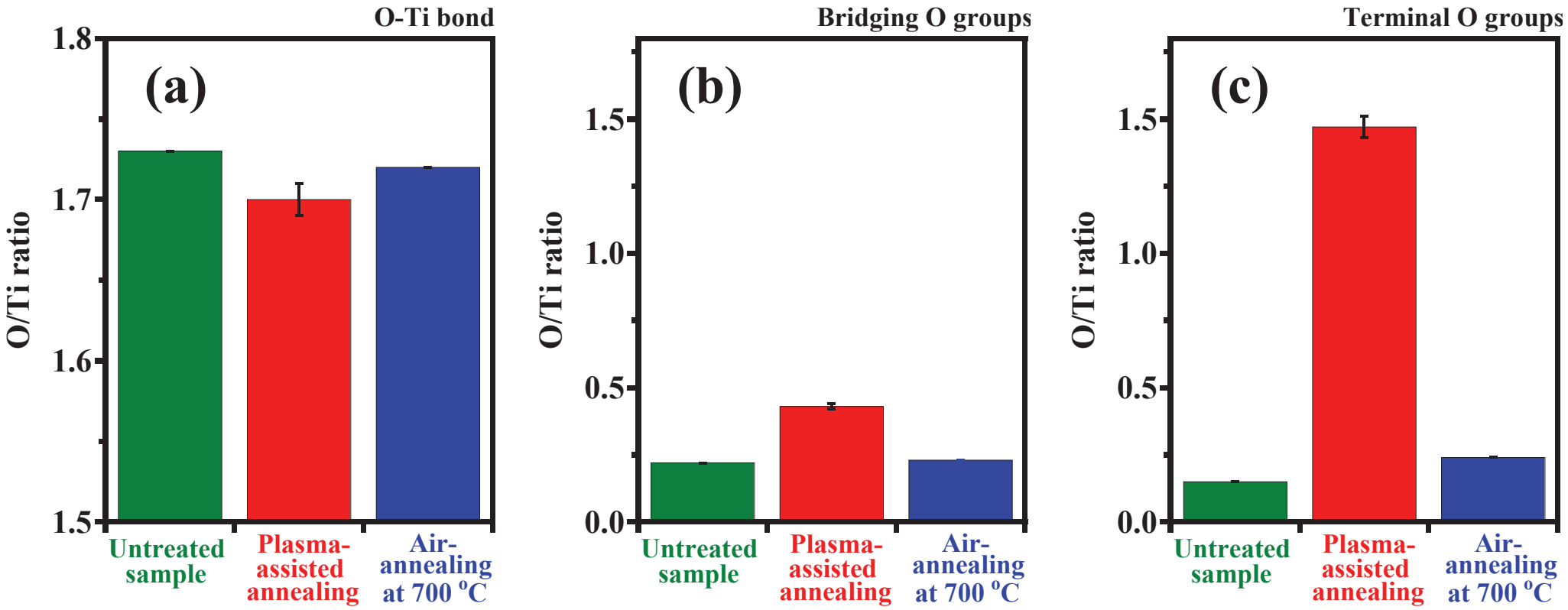

Figure 12. R. Kawakami *et al.*

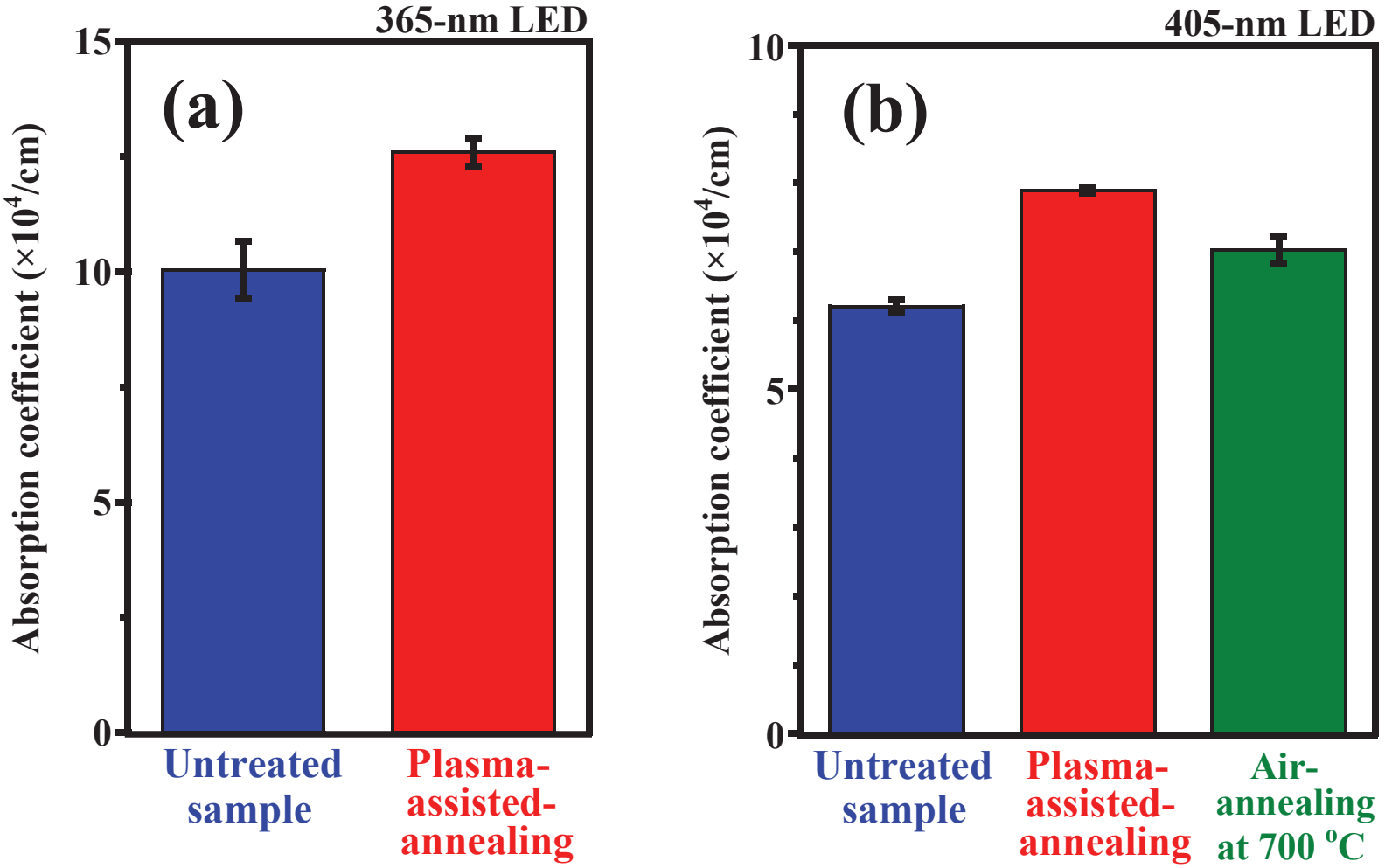

Figure 13. R. Kawakami *et al.*

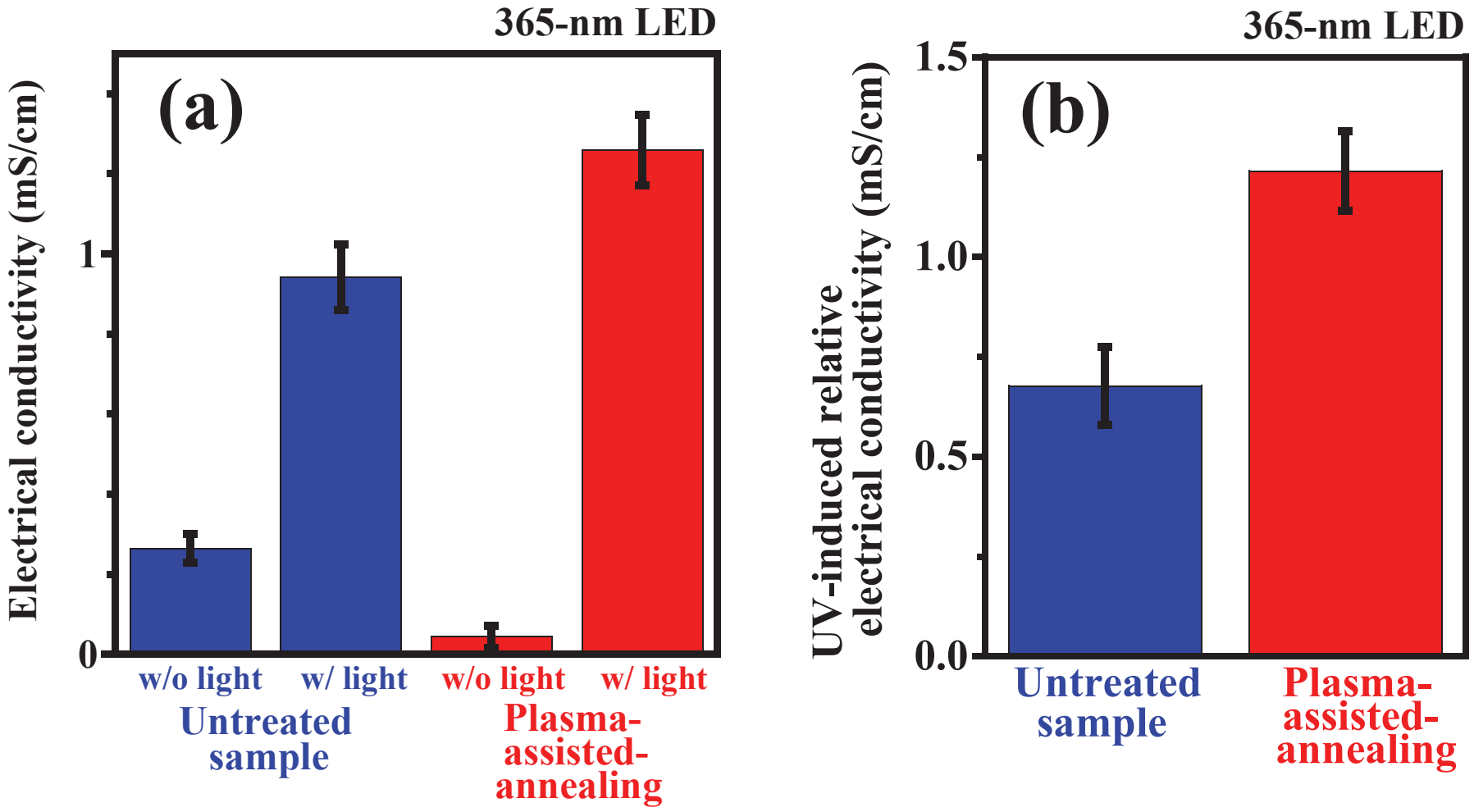

Figure 14. R. Kawakami *et al.*

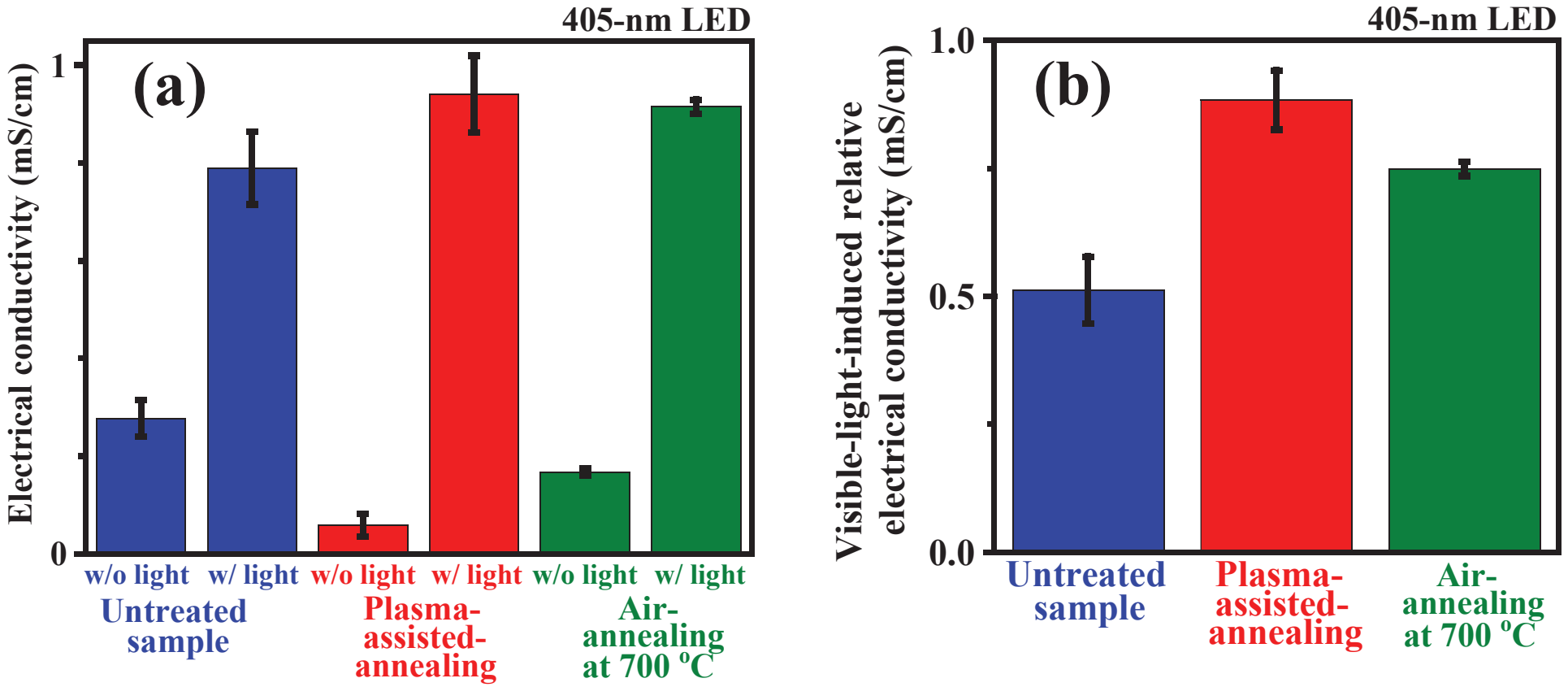

Figure 15. R. Kawakami *et al.*

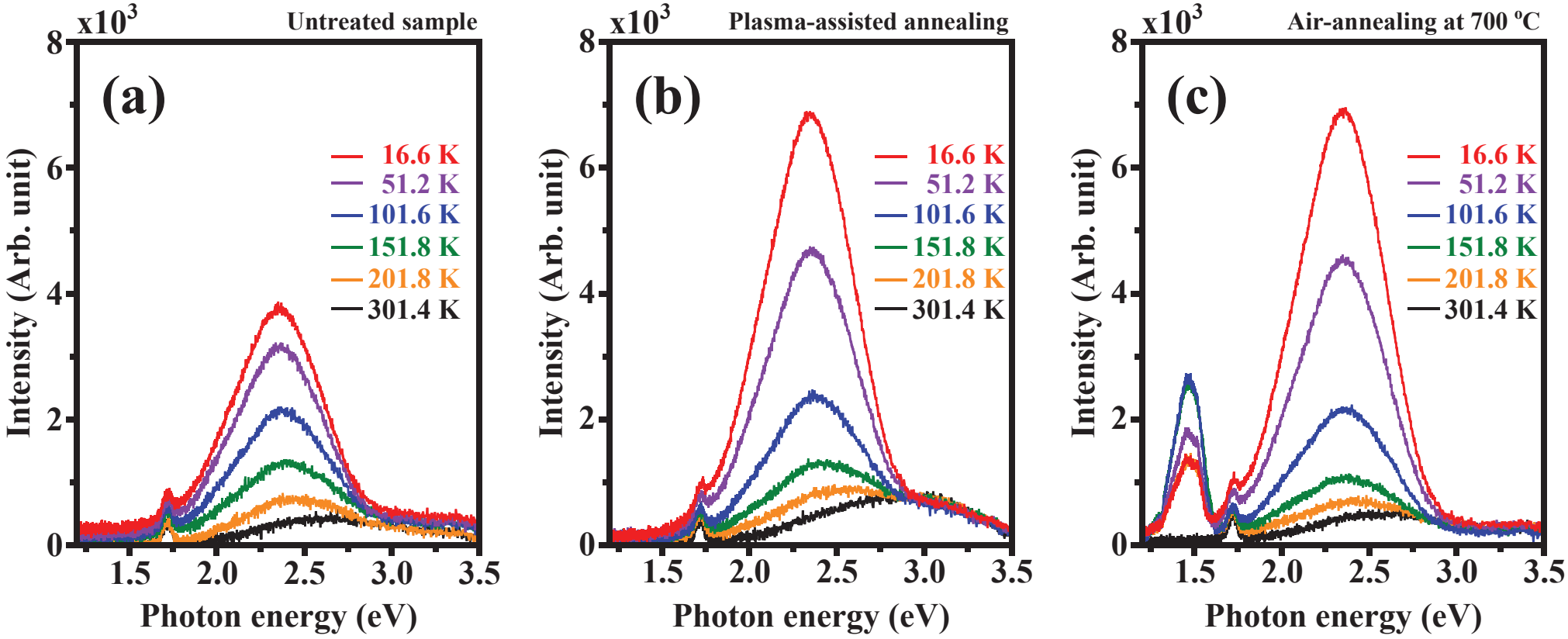

Figure 16. R. Kawakami *et al.*

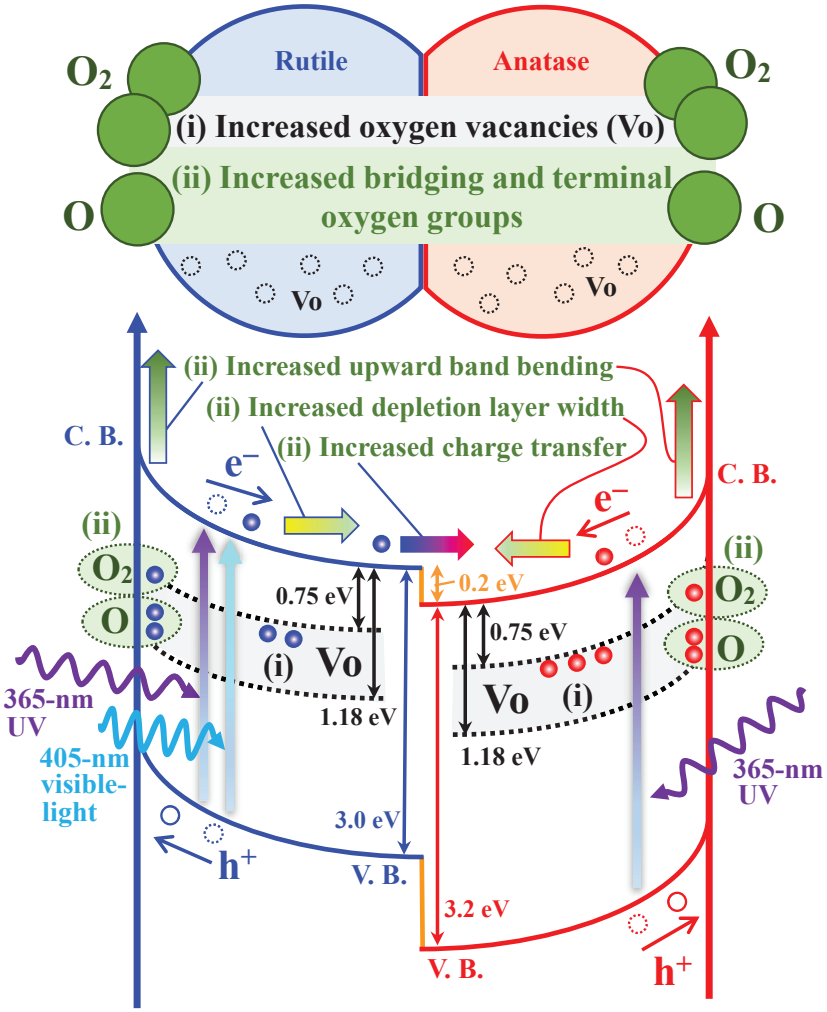

Figure 17. R. Kawakami *et al.*